lubricants

MDPI

Article

Dynamic of a Flexible Rotor-Bearing System Supported by Worn Tilting Journal Bearings Experiencing Rub-Impact

Ebrahim Tofighi-Niaki and Mir Saeed Safizadeh *

School of Mechanical Engineering, Iran University of Science and Technology, Narmak, Tehran 16848, Iran; e_tofighi@cmps2.iust.ac.ir

* Correspondence: safizadeh@iust.ac.ir

Abstract: Wear usually occurs in the loaded part of hydrodynamic bearings and leads to bearing geometry imperfections. This paper investigates the effects of wear-induced geometric imperfections of tilting pad journal bearings (TPJBs) on the dynamic behavior of the system. Furthermore, the effect of wear on the journal-bearing rub-induced contact pressure severity is investigated. A novel tribo-dynamic model is proposed for a flexible rotor-worn TPJB which integrates a mixed elastohydrodynamic model with a rotor-worn TPJB thermal and dynamic model to assess the effects of the bearing wear progression on rotor-TPJB behavior. Based on the results, wear changes the temperature distribution of the pads and oil film as well as the dynamic behavior of the system. Dynamic simulations reveal a higher vibration level and contact pressure for the worn TPJBs near the system's critical speed and service speed. Finally, thermal and dynamic condition indicators are suggested to detect TPJB wear severity at its early stages.

Keywords: rotor dynamics; bearing wear; mixed lubrication; tilting pad journal bearings

1. Introduction

Hydrodynamic journal bearings are used in many high-speed rotating machineries. Among them, tilting pad journal bearings (TPJBs) offer more stability to the system [1]. Hydrodynamic bearings are prone to rub-impact between the journal and the bearing due to their high-speed operation and low clearance between the journal and the bearing. Journal bearings are also exposed to experiencing wear due to insufficient oil film to separate the journal and the loaded part of the bearing in run-up/shot-down phases. Therefore, rub-impact mainly occurs between the journal and loaded pads of TPJBs which can lead to material removal from the inner side of the bearing surface. Therefore, wear-induced geometrical imperfections are formed on the inner side of the loaded pads [2]. As pad pivots tolerate the weight of the rotor, wear-induced geometrical imperfections of the pad are mostly created in front of loaded pad pivots. It is worth mentioning that for the load between pads' (LBP) configuration of the TPJBs, the geometrical imperfection patterns are not equivalent in both loaded pads, since the loaded pad nearer to the journal suffers from more severe wear. These minor geometrical imperfections can negatively affect the TPJB dynamic behavior and change the dynamic behavior of the system at some speeds. For example, they can increase the vibration amplitude of the rotor, resulting in more severe wear and system failure [3]. Therefore, the early detection of journal-bearing contact and subsequent wear-induced bearing geometrical imperfections is crucial in preventing severe failure.

Mathematical simulations and experimental tests have been widely employed in previous studies for the description of the rotor-TPJB behavior. Dimond et al. [4] reviewed the TPJB theory and showed the action of oil film-induced nonlinear forces on the system. The nonlinear behavior of TPJBs has been investigated by several researchers. Cloud et al. [5] presented a five-pad TPJB model and analyzed the effects of two different pad clearances on

check for updates

Citation: Tofighi-Niaki, E.; Safizadeh, M.S. Dynamic of a Flexible Rotor-Bearing System Supported by Worn Tilting Journal Bearings Experiencing Rub-Impact. *Lubricants* **2023**, *11*, 212. https://doi.org/10.3390/lubricants11050212

Received: 7 April 2023
Revised: 2 May 2023
Accepted: 5 May 2023
Published: 8 May 2023

the system stability by numerical simulation and experimental tests. They also showed that numerical simulations over-predict the stability thresholds compared to the experimental results. Although the rotor simulations are verified experimentally by free–free modal tests, a more precise simulation is needed for fluid film bearing to obtain more accurate results. A nonlinear model of flexible rotor-TPJB was presented by Cao et al. [6]. They analyzed the system behavior at equilibrium and numerically obtained the nonlinear dynamic response of the system for a flexible rotor-TPJB model. They did not, however, consider the effects of the temperature-induced oil film viscosity variations on the system equilibrium and dynamic response. The influence of the TPJB cross-coupling stiffness on the system dynamic behavior was analyzed by Synnegard et al. [7]. They explored the effect of considering the TPJB cross-coupling stiffness in the simulation by numerical calculations and verified the results with the experimental bearing displacement values.

Nonlinear forces induced by oil film can lead to chaotic motion and instability in TPJBs. Kim and Palazzolo [8] analyzed the bifurcation diagrams and stability of a five-pad TPJB. They also assessed the effects of oil film nonlinear forces on the quasi-periodic and chaotic motion of the system for a rigid rotor TPJB. The effects of pad preload on dynamic coefficients of the TPJBs were investigated by Dixit and Gupta [9]. They studied the effects of different pad preloads on the system dynamic coefficients and fluid film pressure distribution, but the fluid film temperature changes due to the pad clearance variation were not addressed. Dang et al. [10] presented an experimental procedure for pivot stiffness calculation and showed that pivot stiffness causes a reduction in TPJB dynamic coefficients. Hagemann et al. explored the transition between a fully lubricated condition to partially lubricated condition in TPJBs [11]. They showed that this transition occurs in certain spaces during run-up and shot-down phases, but they did not consider the effect of contact between journal and bearing in these phases.

Various methods have been employed in recent research works to simulate TPJBs. Bizarre et al. [12] used the finite volume method for the thermo-hydrodynamic simulation of a TPJB model. They studied the effects of oil film thickness on temperature and obtained its effects on the temperature distribution of the pads and the eccentricity of the journal. They also verified the simulations with experiments, but the dynamic behavior of TPJBs was not studied. Yan and Huang [13] proposed a thermos-elastohydrodynamic lubrication model that considers the turbulence effect in heavy-load TPJBs to study their static and dynamic behavior. They demonstrated that higher shaft speeds reduce the temperature rise of the pads, and the dynamic characteristics of TPJBs are highly influenced by shaft speed and the direction of the dynamic load. Soltani and Naderan [14] compared an isothermal 3D model of a TPJB with conventional 2D model and concluded that the results of 3D and 2D models are almost matched for heavier rotor with higher eccentricities. At lower eccentricities, a greate significant difference can be detected between the 3D and 2D models of the oil film. Therefore, the 2D model of the oil film could well identify the TPJB behavior for heavy rotors at higher shaft eccentricities. This paper failed to analyze the effect of temperature on the oil film behavior. Wanger and Allaire examined the effect of the pad pivot flexibility on the system frequency response in combination with the oil film effect [15]. Han et al. [16] investigated the impact of the turbulent flow of lubricant on the dynamic coefficients of TPJBs by perturbing the TPJB turbulence model. They found that neglecting turbulent coefficients in the calculation of TPJBs' dynamic coefficients results in an overestimation of the obtained results. However, perturbed viscosity can be neglected for simplification in calculations. Hojjati et al. [17] used the pad perturbation method to obtain both the linear and nonlinear dynamic coefficients of TPJBs. They showed that large eccentricities have a significant effect on TPJBs' nonlinear dynamic coefficients and that an increase in preload leads to an increase in both linear and nonlinear dynamic coefficients. Furthermore, Jin et al. [18] investigated the pivot stiffness effect on the vibration amplitude of TPJBs and showed that pivot stiffness leads to reduced resonance and working amplitude of the system. Finally, Shin et al. [19] published a review paper on thermal modeling methods for journal-bearing systems. They did not mention any previous works which simulated the

effect of temperature-induced variations of the oil film viscosity on the dynamic behavior of a rotor-worn TPJB.

The nonlinear behavior of hydrodynamic bearings due to oil film forces can be affected by geometrical imperfections in journal and bearing. Bearing geometrical imperfections are created as a result of manufacturing error and wear during the service time of the system. Wear can increase the loaded pads' clearance and preload, and therefore, change the system behavior. Dufrane et al. [20] measured wear depth on a worn plain bearing and suggested a mathematical relation to modify the oil film thickness formula in the worn area of the bearing. Gertzos et al. [21] presented a computational model to simulate wear in hydrodynamic plain bearings. They analyzed the eccentricity ratio changes, friction coefficient, attitude angle, and side oil flow versus the wear depth. Furthermore, The effect of wear was explored on the dynamic response of a rotor-bearing system by Chasalevris et al. [22]. According to their study, wear in the bearing is the source of additional harmonics in the frequency response of the system. They used continuous wavelet transform for wear detection in a plain bearing. Machado and Cavalca [23] investigated the effects of hydrodynamic plain bearing wear on oil film pressure distribution, dynamic coefficients, and vibration amplitude. They reported an increase in journal-worn bearing vibration amplitude due to the bearing wear. Alves et al. [24,25] developed a model to describe wear in journal-hydrodynamic bearings. They used temperature and the system vibration spectral analysis to determine the severity of wear in plain bearings and concluded that wear increments the system's anisotropy. Furthermore, they showed that wear-induced system anisotropy is more detectable in lower speeds as the rotor has higher eccentricity and rotates near the bearing.

The solid-to-solid contact between journal and the bearings is one of the main sources of hydrodynamic bearings wear and the bearing geometric imperfections induced by wear. Journal-bearing contact may occur due to several reasons such as slow operating speed or high mass imbalance of the rotor. Inclusion of the journal-bearing contact effect on the dynamic behavior of the system can lead to a more accurate simulation of the dynamic motion of the system which can be utilized for system fault diagnosis. The effects of the oil film in the contact region should be considered for precise simulation of the journal-bearing contact. To this end, a mixed elastohydrodynamic model can be implemented by assuming that surfaces are nominally smooth with a specified roughness. The solid-to-solid contact force is created due to contact between the asperity summits. In a journal-bearing contact region, the oil film flows between the journal and the bearing surface asperities. This lubrication regime is called mixed-lubrication which was used by Kazama and Naritia [26] to assess the effects of the wear-induced bearing geometrical imperfections on the solid-to-solid contact between a journal and a hydrodynamic plain bearing. They also obtained the oil film pressure distribution and the extent of the effect of bearing wear on a journal-worn bearing behavior at its equilibrium state. They, however, did not address the effect of bearing geometrical imperfections and journal-bearing contact on the dynamic behavior of the system. Varney and Green [27] applied the mixed-lubrication theory to simulate the dynamic behavior of a rotor-circular stator experiencing rotor-stator rub-impact. They assumed the rotor and stator surfaces are rough and used asperity contact forces to simulate the rotor-stator contact. Xiang et al. [28] simulated the interaction between wear and fluid-solid-thermal coupling in a sleeve lubricated bearing. They investigated the effect of the surface roughness to calculate solid-to-solid contact force in addition to examining the nonlinear behavior of a water lubricated bearing using a mixed-thermoelastohydrodynmaic lubrication model for the lubricant film [29]. They only studied the plain bearings and did not address the TPJBs' behavior. Cai et al. [30] developed a mathematical model for coupled bearings using mixed lubrication theory. They investigated the effect of contact between coupled bearings and demonstrated that an increase in the length-to-diameter ratio of the journal-bearing leads to a decrease in the asperity contact force in their model. Guo et al. [31] implemented the mixed lubrication theory to simulate a misaligned rotor-bearing system that experiences journal-bearing contact. They also considered the oil film

temperature effect on the lubricant viscosity and pressure distribution and verified the results experimentally. They, however, did not investigate the journal-bearing dynamic motion in a mixed lubrication regime. Xiang et al. [32] proposed a method for modifying the bearing surface profile to reduce wear and asperity contact. They found that the thermal behavior of the presented model does not have a significant effect on journal-bearing wear. However, the effectiveness of the profile modification method depends on the bearing design parameters.

In addition to the journal-bearing solid-to-solid contact and wear, which lead to bearing geometrical imperfections, manufacturing error is another source of journal-bearing geometrical imperfections. Dang et al. [33] simulated the effect of TPJB geometric imperfections due to manufacturing errors. They investigated the effects of pad radius variations on a TPJB equilibrium position and the lubricant pressure distribution while neglecting the effect of TPJB geometric imperfections on the dynamic motion of the system. Lee et al. [2] explored the effects of the use of worn pads on a TPJB equilibrium position. As wear mostly occurs at low speeds due to the lack of adequate oil film to separate the journal and the bearing, they created an artificial geometrical imperfection on the loaded pads and analyzed the effects of geometrical imperfections on the temperature distribution of the worn pads. They also found the journal equilibrium position both numerically and experimentally. They reported an increase and a decline in the temperature of the loaded pads and upper pads, respectively. Zhang et al. [34] experimentally investigated the effects of wear in pads and the journal geometrical imperfections on the behavior of TPJBs. They observed that bearing geometrical imperfections change the system vibration level at some speeds but they did not study the dynamic behavior of the system in frequency domain. Silva and Nicoletti [35] studied the effects of uncertainty due to assembly error in pad clearances on the system dynamic coefficients. They showed that bearing asymmetry can cause an increase or decrease in TPJB dynamic coefficients. Furthermore, Lou et al. [36] showed that small uncertainties in pivot position and pad angular extension do not have a significant effect on static characteristic of TPJB, whereas uncertainties in shaft radius, pad inner radius, and pivot radius in a specified preload could have a considerable influence on TPJB static characteristic. They did not study the effect of TPJB geometric uncertainties on the dynamic characteristic of the system.

Wear in TPJBs can change the dynamic motion of the system, therefore, monitoring the vibration component variations can be used as a tool to detect wear in journal-bearings at its early stages. Ranjan et al. [37] employed wear debris, vibration, and temperature analysis to experimentally study the wear and journal-bearing rub-impact in a water lubricated TPJB. They mentioned a considerable increase in the amplitudes of 5X and 10X frequency component in the system vibration signals due to wear and metal-metal contact between the journal and the bearing. Zhou et al. [38] also showed that water lubricated TPJB, which operates in mixed lubrication regime, experiences a lower contact load in heavy load conditions in comparison with conventional water lubricated bearings. Dixit and Gupta [39] used the short bearing assumption to evaluate the effects of the TPJB geometrical parameters on the oil film dynamic coefficients. They showed that an increase in bearing clearance changes the oil film stiffness but did not consider the effect of possible contact between journal and bearing which may occur as a result of variations in the bearing stiffness. The effects of geometrical imperfections of the TPJB bearing on the dynamic behavior of the system was studied before [40], while neglecting the effect of the oil film temperature variations due to the bearing geometrical imperfections on the system dynamic coefficients and the effect of bearing wear on the rotor-bearing contact pressure severity. According to Lee et al. [2], the wear-induced geometric imperfections of the loaded pad can alter the temperature distribution on the pads and the lubricant film. Therefore, these temperature changes will affect oil film viscosity and the journal-bearing dynamic behavior.

Based on the provided literature review, no study has addressed the impact of the wear-induced variations in the TPJB temperature on the dynamic behavior of the system. Furthermore, previous works did not examine the effect of the TPJBs' geometric imperfec-

tions on journal-bearing rub-impact severity. This paper is thus aimed to analyze the effects of the TPJBs' geometric imperfections and wear severity on the dynamic and thermal behavior of the system. Moreover, their effects were assessed on rub-impact severity between the journal and the bearing. Therefore, the presented simulations require three major parts. Firstly, a rotor supported by intact TPJBs is simulated. Then, the effect of wear-induced bearing geometric imperfections is added to the model. Finally, the contact between the journal and the bearing is simulated and added to the model. Therefore, the novelty of this work can be described as follows: (1) A tribo-dynamic model is presented to investigate the effects of wear-induced TPJB geometrical imperfections on the thermal and dynamic behavior of the system. This model is then utilized to evaluate the temperature distributions of the lubricant and pad for intact and worn TPJBs. (2) The effect of TPJB geometrical imperfection on journal-bearing rub-impact severity is then analyzed for different wear severities to evaluate the effect of bearing geometrical imperfection on subsequent journal-bearing rub-impact. (3) The effects of journal-worn TPJB rub-impact on the dynamic motion of the system is explored using the proposed model and dynamic indicators suggested to detect wear at its early stages. The details of the proposed mathematical model are presented in Section 2. Section 3 discusses the results while the validation of the proposed model is given in Appendix A.

2. Theory

2.1. Mathematical Model Description

In this research, a flexible rotor-tilting pad journal bearing (TPJB) dynamic behavior is simulated considering the bearing geometrical imperfections. Figure 1 illustrates the presented model for the flexible rotor and TPJBs. In this model, the five pad TPJBs are numerically simulated to obtain the equivalent damping and stiffness coefficients at the equilibrium position of the system. The dynamic coefficients are used to calculate the critical speeds of the flexible rotor and the system behavior at its equilibrium state. Furthermore, the TPJBs' hydrodynamic and solid-to-solid contact forces were determined at different wear severities for an unbalanced rotor-TPJB system. The equations of motion of the rotor-TPJB system can be written as follows [41]:

$$[M_s]\{\ddot{u}\} + \omega[G]\{\dot{u}\} + [K_s]\{u\} = \{F_{unb}\} + \{F_g\} + \{F_{nl}\} \tag{1}$$

$$J\ddot{\delta}_{p,l} = M_l, \qquad l = 1, \ldots, N_{pads} \tag{2}$$

$$J\ddot{\delta}_{p,r} = M_r, \qquad r = 1, \ldots, N_{pads} \tag{3}$$

where $[M_s]$, $[K_s]$, and $[G]$ are the shaft mass, stiffness, and gyroscopic matrices, respectively. The force induced by the rotor mass imbalance, gravity force, and the nonlinear forces applied on the rotor are represented by $\{F_{unb}\}$, $\{F_g\}$, and $\{F_{nl}\}$, respectively. Moreover, J and δ_p in Equations (1)–(3) stand for the p'th pad moment of inertia and tilt angle, respectively. Indices l and r are used for pad numbering in the left and the right bearings, respectively. The pad numbers are shown in Figure 1. In this study, hydrodynamic TPJBs with pad geometric imperfections are simulated, considering the effects of journal-bearing rub-impact on the system motion. The nonlinear force $\{F_{nl}\}$ on the rotor consists of the oil film hydrodynamic force and the rotor-bearing solid-to-solid contact force. The solid-to-solid contact force applies when the contact between the journal and the bearing occurs. Rotor-bearing contact may happen due to the high level of rotor vibration or the lack of sufficient oil film to separate the journal and bearing. Horizontal and vertical components of the nonlinear forces are calculated as follows [41]:

$$F_x = -\sum_{1}^{N_{pads}} \left[\int_{-\frac{L}{2}}^{\frac{L}{2}} \int_{\theta_{s,p}}^{\theta_{e,p}} \left(\left(P_{fld,p} + P_{c,p} \right) \cos\theta - sign\left(\left(\vec{V}_1 - \left(\vec{V}_{2,p} \cdot \vec{e} \right) \vec{e} \right) \cdot \vec{e} \right) \left(\tau_{fld,p} + \tau_{c,p} \right) sin\theta \right) R_j d\theta dz \right] \tag{4}$$

$$F_y = -\sum_{1}^{N_{pads}} \left[\int_{-\frac{L}{2}}^{\frac{L}{2}} \int_{\theta_{s,p}}^{\theta_{e,p}} \left(\left(P_{fld,p} + P_{c,p} \right) \sin\theta - sign\left(\left(\vec{V}_1 - \left(\vec{V}_{2,p} \cdot \vec{e} \right) \vec{e} \right) \cdot \vec{e} \right) \left(\tau_{fld,p} + \tau_{c,p} \right) \cos\theta \right) R_j d\theta dz \right] \quad (5)$$

where F_x and F_y constitute the nonlinear force components in x and y directions, respectively. $P_{fld,p}$ and $P_{c,p}$ are the oil film hydrodynamic pressure and the contact pressure between the journal and the bearing, respectively. Moreover, the shear stresses due to the oil film hydrodynamic pressure and the contact pressure are represented by $\tau_{fld,p}$ and $\tau_{c,p}$, respectively. Other parameters in Equations (4)–(5) include the pad starting angle, the pad ending angle, the pad circumferential angle, the journal surface speed, the p'th pad surface speed, and the pad axial length are depicted by θ_s, θ_e, θ, $\vec{V}_1$, $\vec{V}_{2,k}$, and L, respectively. Furthermore, $\vec{e}$ denotes the unit vector in the journal absolute velocity direction at the journal-bearing contact. The moment applied from the oil film hydrodynamic force and the journal-bearing solid-to-solid contact force on the pivot of the p'th pad can be determined by Equation (6) as follows [41]:

$$M_p = -\int_{-\frac{L}{2}}^{\frac{L}{2}} \int_{\theta_{s,p}}^{\theta_{e,p}} \left[-\left(R_j + t_p \right) \left(\theta - \theta_{p,k} \right) \left(P_{fld,p} + P_{c,p} \right) - sign\left(\left(\vec{V}_1 - \left(\vec{V}_{2,p} \cdot \vec{e} \right) \vec{e} \right) \cdot \vec{e} \right) \left(\tau_{fld,p} + \tau_{c,p} \right) t_p \right] \cos\left(\theta - \theta_{p,k} \right) R_j d\theta dz \quad (6)$$

where M_p is the applied moment on the p'th pad pivot, θ_p denotes the p'th pad pivot angle, and t_p shows the thickness of the p'th pad. Forces and moments should be calculated for the journal position at each time step. The methods used for calculating the effect of the bearing geometric imperfections, oil film hydrodynamic pressure, and contact force are described in the following section.

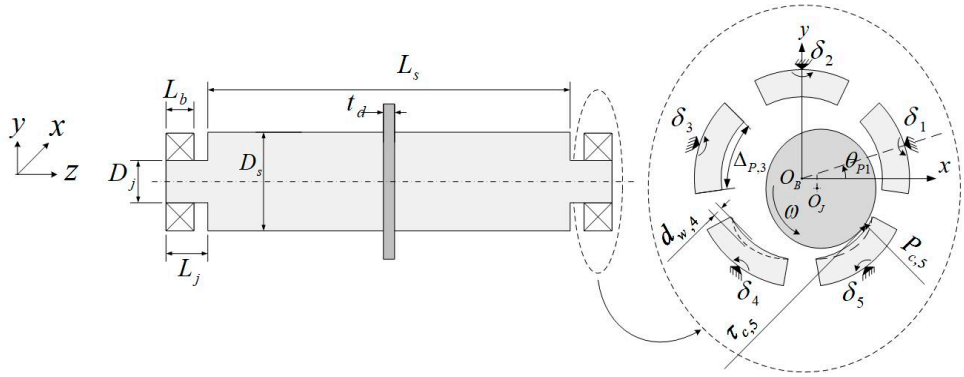

Figure 1. Flexible rotor-worn tilting pad journal bearing model.

2.2. Tilting Pad Bearing Geometric Imperfections

Bearing imperfections can occur due to several reasons such as manufacturing errors, assembling errors, and wear. These imperfections can be modeled as uncertainties to analyze system behavior and obtain a reliable range for bearing imperfections [35,42]. This work investigates the effect of geometric imperfections in TPJBs induced by wear. Journal-bearing wear occurs when the oil film formed on the loaded parts of the bearing is not sufficient to separate the journal and the bearing. This situation happens when the rotor speed is not high enough for sufficient oil film formation during the run-up and shot-down phases. Journal-bearing contact leads to the removal of the bearing material from the inner side of the loaded pads and subsequent pad geometrical imperfections. The worn pad material removal at low speeds almost occurs on the pad's inner side and in front of the pad pivot [2]. In this study, it is assumed that TPJB geometric imperfections are induced by contact between the journal and the loaded pads during the run-up/shot-down phases. The effects of using worn pads with different wear severities on the system thermal and dynamic behavior are studied. The simulated TPJB has the load between pads (LBP) configuration. Since the rotor does not rotate in the middle of the bearing, wear severity is not equal on both loaded pads, as the pad closer to the journal center experiences more severe wear. It is assumed that the rotor rotates in the counter-clockwise direction, and

there are five pads installed in the bearing. The pads' numbering is depicted in Figure 1. In this case, the pads No. 4 and 5 experience journal-bearing wear and the journal equilibrium position will be closer to pad No. 5. Therefore, pad No. 5 experiences more severe wear. Moreover, the maximum wear depth on the fifth pad is assumed to be twice that of the fourth pad. A schematic representation of pad No. 5 with wear signature on its inner side is depicted in Figure 2. A wear pattern for TPJBs with LBP configuration is proposed by Lee et al. [2]. Based on the proposed wear pattern, wear occurs on the loaded pads of TPJBs, and the maximum wear depth is observed in front of the pad pivot. In this work, the presented mathematical model for worn hydrodynamic bearings in [3] is considered and modified for TPJBs with LBP configuration based on the proposed TPJB wear pattern in [2]. Therefore, the oil film thickness on the p'th pad of the TPJB, considering the worn pads' geometrical imperfections, can be determined by:

$$\bar{h}_p = \begin{cases} \bar{h}_{0,p}(\theta), & p = 1,2,3 \\ \bar{h}_{0,p}(\theta) + d_{w,p}(\theta), & p = 4,5 \end{cases} \tag{7}$$

where:

$$\bar{h}_{0,p}(\theta) = (R_p - R_j) - X_j \cos\theta - Y_j \sin\theta - (R_p - R_b)\cos(\theta - \theta_p) - \delta_p(R_p + t_p)\sin(\theta - \theta_p) \tag{8}$$

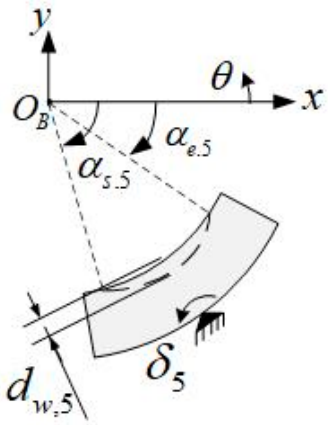

Figure 2. Pad number 5 schematic considering pad geometrical imperfections induced by wear.

In Equation (8), R_p and R_b represent the pad and the bearing radii, respectively. Furthermore, wear depth for a worn pad is denoted by $d_{w,p}$ which can be obtained by the formulation presented in [3]. Since the maximum wear depth occurs in front of the pivot [2], this formulation should be modified for TPJBs as follows:

$$d_{w,p} = \begin{cases} d_{max,p} - C_b(1 - \cos(\theta - \theta_p)), & \alpha_{s,p} < \theta < \alpha_{e,p} \\ 0, & otherwise \end{cases} \tag{9}$$

where $\alpha_{s,p}$ and $\alpha_{e,p}$ are the starting and ending angle of wear on the p'th pad with the following expressions:

$$\alpha_{s,p} = \frac{\pi}{2} + \cos^{-1}\left(\frac{d_{max,p}}{C_b} - 1\right) + \theta_p \tag{10}$$

$$\alpha_{e,p} = \frac{\pi}{2} - \cos^{-1}\left(\frac{d_{max,p}}{C_b} - 1\right) + \theta_p \tag{11}$$

Noteworthy, wear profile depends on diverse factors such as application, rotating direction, manufacturing errors, and the system properties. The wear signature on pads is presented in Equations (9)–(11) as an assumption for TPJB wear, but the wear sig-

nature may differ in practical measurements based on the operating conditions of the system. Sharma [43] discussed different methods, such as bearing inner diameter and out-of-roundness measurement, to obtain the hydrodynamic bearing wear signature. The out-of-roundness measurement method was proposed as an effective method for wear measurement in the early stage. The presented wear profile can be replaced by any other profile of wear and can be used in the proposed worn TPJB model. The other wear signatures can be obtained using wear depth measurement on the worn bearings or using other mathematical models for wear. Some examples of other wear signatures are given in [2,26].

2.3. Tilting Pad Bearing Thermo-Hydrodynamic Simulation

Hydrodynamic pressure distributions on each pad of a TPJB are obtained by the Reynolds equation. The mixed lubrication and the oil film turbulence may affect the behavior of the TPJBs experiencing heavy and impact loads [44]. Therefore, a modified version of the Reynolds equation considering the effects of surface roughness and the fluid turbulence on the oil film flow is provided in Equation (12) [45]:

$$\frac{\partial}{\partial\theta}\left(\phi_\theta^p\frac{\bar{h}_p^3}{k_\theta\mu}\frac{\partial P_{fld,p}}{\partial\theta}\right)+\frac{\partial}{\partial z}\left(\phi_z^p\frac{\bar{h}_p^3}{k_z\mu}\frac{\partial P_{fld,p}}{\partial z}\right)=\frac{V_1+V_2}{2}\frac{\partial\left(\rho\bar{h}_{T,p}\right)}{\partial\theta}+\frac{V_1-V_2}{2}\frac{\sigma\partial\phi^s}{\partial\theta}+\frac{\partial\left(\rho\bar{h}_p\right)}{\partial t} \tag{12}$$

where $\bar{h}_p$ and $\bar{h}_{T,p}$ are the oil film thickness on the p'th pad and the expected value of the mean gap between the journal and the p'th pad, respectively. The standard deviation of the surface asperity height on the rough surface of the journal and the bearing is also denoted by σ. For large enough distances between the journal and the pad's inner surface, the effect of surface roughness can be neglected, and the expected mean gap value $\bar{h}_{T,p}$ is equal to the oil film thickness $\bar{h}_p$. In the cases where the separation between the journal and the pad's inner surface is less than 3σ, the surface roughness affects the mean gap value and the mean gap will be equal to the expected value of $\bar{h}_{T,p}$, considering the surface roughness effect. In this work, it is assumed that asperities have Gaussian distribution on both journal and pads. The formulation for calculating the expected value of $\bar{h}_{T,p}$, considering the effect of Gaussian distribution of the asperities, is given in [46]. Furthermore, the oil film viscosity and density are represented by μ and ρ, respectively, while ϕ_θ^p, ϕ_z^p, and ϕ^s are the oil flow correction factors. The effects of surface roughness on oil film flow can be evaluated by these factors. The value of the oil flow correction factors depends on the surface roughness pattern and asperities heights. Patir and Cheng [46] presented a detailed description of the calculation procedure for oil flow correction factors. The effects of oil film turbulence can be obtained by k_θ and k_z factors which can be calculated as follows [47]:

$$\begin{cases} k_\theta = 12\left(1+TBA.R_L^{ETA}\right) \\ k_z = 12\left(1+TBB.R_L^{ETB}\right) \\ k_\theta = k_z = 12 \end{cases} \quad \begin{matrix} Turbulent\ Flow \\ \\ Laminar\ Flow \end{matrix} \tag{13}$$

where TBA, TBB, ETA, and ETB are Ng-Pan [47] turbulent model constants as listed in Table 1. R_L is the local Reynolds number.

Table 1. Ng-Pan turbulence model constants [47].

Model	TBA	ETA	TBB	ETB
Ng-Pan	0.00113	0.9	0.000358	0.96

Boundary conditions for the oil film pressure distribution in a hydrodynamic TPJB can be written as:

$$P_{fld,p}(\theta_s,z)=P_{fld,p}(\theta_e,z)=P_{fld,p}\left(\theta,\pm\frac{L}{2}\right)=P_{\sup} \tag{14}$$

Reynolds equation given in Equation (12) can be solved using the finite element method based on the boundary conditions in Equation (14). Reynolds boundary condition is also applied on Equation (12) to consider cavitation effects in model [2]. Pad surfaces are meshed via quadrilateral elements. The Galerkin method is used to obtain the hydrodynamic pressure on each node. A detailed description of the finite element solution of the Reynolds equation can be found in [48].

It should be noted that the oil film viscosity varies by film temperature as follows [49]:

$$\mu = \mu_0 \exp\left(-\beta\left(T_p - T_0\right)\right) \tag{15}$$

where μ_0 is oil film viscosity at the temperature of T_0, β shows the thermo-viscosity index, and T_p denotes the lubricant temperature in the p'th pad. Due to the small oil film thickness compared to the pad's circumferential dimension and the nearly constant temperature of the lubricant in the axial direction, the one-dimensional energy equation is employed. Therefore, the iterative solution of the one-dimensional energy equation and the two-dimensional heat equation is used to determine the lubricant and pad's temperature distributions [48–50]. Then, the calculated oil film temperature distribution is used to obtain the oil film viscosity. The lubricant temperature on the p'th pad, T_p, can be determined based on the one-dimensional energy equation as follows [49]:

$$\rho \overline{C}_p \frac{\omega}{2} \frac{dT_p}{d\theta} = \frac{\mu \left(R_j \omega\right)^2}{\left(\overline{h}_p\right)^2} - \frac{H_{p1}\left(T_p - T_p^b\right) + H_j\left(T_p - T_j\right)}{\overline{h}_p} \tag{16}$$

where ρ and $\overline{C}_p$ are the oil film density and specific heat capacity, respectively. Furthermore, T_j and T_b^p respectively represent the temperatures of the journal and the p'th pad which could be obtained using the calculated lubricant temperature as follows [49].

$$T_j = \frac{\sum_{p=1}^{N_{pads}} \int_{\theta_{s,p}}^{\theta_{e,p}} T_p d\theta}{N_{pads} \Delta_p} \tag{17}$$

The two-dimensional heat equation which gives the pads temperature distribution is given as follows:

$$\frac{1}{r}\frac{\partial}{\partial r}\left(r\frac{\partial T_p^b}{\partial r}\right) + \frac{1}{r^2}\frac{\partial^2 T_p^b}{\partial \theta^2} = 0;\ R_p \le r \le R_p + t_p, \theta_{s,p} \le \theta \le \theta_{e,p} \tag{18}$$

It is worth mentioning that the boundary conditions of Equation (18) include the conduction heat transfer in the pads, convection heat transfer between the oil film and the pad's inner side, and convection heat transfer between the air, the pad's edges and the pad's backside [49].

In this paper, the finite difference method is used to solve the one-dimensional energy equation, while the finite element method is implemented to solve the two-dimensional heat conduction equation in pads (see Equations (16) and (18)). The following suggestion is used to calculate the lubricant temperature at the leading edge of each pad [49]:

$$T^p\left(\theta_{s,p}\right) = T_{\sup} + \frac{\min\left(\left\{\overline{h}_k(\theta_{s,k})\right\}_{k=1,\ldots,N_{pads}}\right)}{\overline{h}_p\left(\theta_{s,p}\right)} \Delta T;\ p = 1, \ldots, N_{pads} \tag{19}$$

where ΔT is the oil film bulk temperature rise, and T_{sup} shows the oil film supply temperature. The lubricant film bulk temperature rise can be determined by [49]:

$$\Delta T = \frac{\sum_{p=1}^{N_{pads}} R_j \omega \int_{\theta_{s,p}}^{\theta_{e,p}} \mu \frac{R_j \omega}{\overline{h}_p} L R_j d\theta}{Q_{\text{sup}} \rho \overline{C}_p} \tag{20}$$

Equations (12), (16) and (18) should be solved iteratively to obtain the lubricant viscosity at the TPJB equilibrium position. The oil film viscosity can be finally calculated via Equation (15). A more detailed description of the iterative procedure for energy and heat conduction equation solution can be found in [49].

2.4. Contact Pressure

The hydrodynamic and solid-to-solid contact pressure must be calculated simultaneously to obtain the contact pressure between two lubricated surfaces. It is assumed that the journal and the bearing surfaces are rough and covered by asperities. Moreover, the combined standard deviations of the asperity heights on both surfaces are assumed to be σ. The lubrication regime of the system can be evaluated based on the $\overline{h}_p/\sigma$ ratio. For $\overline{h}_p/\sigma > 3$, the journal and the bearing are far enough to neglect the surface roughness effect. In such conditions, the system works in the hydrodynamic lubrication regime. There is no solid-to-solid contact pressure between two surfaces that operate in this lubrication regime. If $0.5 < \overline{h}_p/\sigma < 3$, the asperities come to contact with each other, and solid-to-solid contact pressure affects the system behavior. At the same time, oil film flows between the asperities whose flow rate will be under the influence of the asperities. This regime is called the mixed lubrication regime [46]. The presented model by Greenwood and Williamson [51] is used to obtain solid-to-solid contact pressure in this situation. Johnson et al. [52] utilized this model for contact pressure calculation in lubricated surfaces. Hence, the elastic and plastic contact pressure induced by journal-bearing contact can be obtained using the following relations [26]:

$$P_e = \frac{2}{3} E' \eta \beta' \sigma^* \left(\frac{\sigma^*}{\beta'}\right)^{\frac{1}{2}} \left[F_{\frac{3}{2}}\left(d^*_{e,p}\right) - F_{\frac{3}{2}}\left(d^*_e + w^*_p\right)\right] \tag{21}$$

$$P_P = \pi H_a \eta \beta' \sigma^* F_1\left(d^*_e + w^*_p\right) \tag{22}$$

$$P_{c,p} = P_e + P_P \tag{23}$$

In Equations (21)–(23), the standard deviation of the asperity summit height is depicted by σ^* which is equal to 0.7σ [52]. Surface-equivalent Young modulus, the asperities density, and the asperities summit radius are depicted by E', η, and β', respectively. Furthermore, P_e denotes the contact pressure induced by the elastic deformation of asperities, while P_P shows the contact pressure induced by the plastic deformation of the asperities. $P_{c,p}$ is the total pressure due to the contact between two rough surfaces on the p'th pad. In Equations (21)–(23), $w^*_p = (\beta'/\sigma^*)(2H_a/E')^2$ is the plasticity index, while H_a represents the hardness of the softer material and $d^*_{e,p}$ represents the non-dimensional separation between the two rough surfaces. The separation between the two rough surfaces can be obtained as follows [26]:

$$d^*_{e,p} = H_p \; if \; H_p \geq 1.8 \tag{24}$$

$$d^*_{e,p} = 1.5H_p - 0.9 \; if \; H_p < 1.8 \tag{25}$$

In Equations (21)–(23), F_m is the probability of contact between the asperity summits of the two rough surfaces which can be determined by:

$$F_m(h_s) = \int_{h_s}^{\infty} (s - H_p)^m \varphi(s) ds \tag{26}$$

where $\varphi(s)$ is the probability distribution function. The Gaussian asperity distribution is considered in this research as most of the engineering surfaces have this distribution. $\varphi(s)$ can be expressed as [26]:

$$\varphi(s) = (2\pi)^{-\frac{1}{2}} \exp\left(-\frac{s^2}{2}\right) \tag{27}$$

It is worth mentioning that the F_m values can be determined by numerical integration. A mathematical equation that states the F_m numerical values is given by Haneef et al. [53]. The effect of hydrodynamic bearing wear on the changes in the asperity distribution pattern is studied by Ma et al. [54]. In this work, a standard deviation of 0.4 µm is used for asperity heights and the maximum wear depth is assumed to be 20 µm. Thus, it is assumed that any changes in the asperity distribution pattern induced by wear are negligible when compared with the effect of bearing geometry imperfections. Therefore, the asperity distribution is assumed to be unchanged in both the intact and worn bearing cases.

To sum up, Equations (12) and (21)–(23) are used to obtain the hydrodynamic and the contact pressure between the journal and the bearing in the hydrodynamic and mixed lubrication regimes. Then, the system response is calculated using Equations (1)–(3) to consider the effects of journal-bearing contact on a TPJB dynamic behavior.

3. Results and Discussion

This paper is an attempt to study the effects of rotor-tilting pad journal bearing (TPJB) contact and bearing geometrical imperfections. Furthermore, the effects of worn pad geometrical imperfections are explored on the thermal and dynamic behavior of the system and, rub-impact between the journal and the bearing is also analyzed. Table 2 shows the properties of a flexible rotor-TPJB system, considered for mathematical simulation of this work. TPJB surface and thermal properties are also given in Table 3.

Table 2. Rotor-tilting pad bearing properties.

Rotor		Bearing	
Parameter	**Value**	**Parameter**	**Value**
E_S	200 Gpa	f_p	0.5
ρ_s	8000 kg/m^3	D_b	125.196 mm
N	0.3	L	50 mm
D_j	125 mm	m	0.3988
D_s	160 mm	θ_p	18, 90, 162, 234, 306 deg
L_s	1.84 m	Δ_p	52 deg
t_d	0.08 m	J_p	0.0024 kg/m^3
m_d	176.4 kg	m_j	1200 kg

Table 3. TPJB Thermal and Surface properties.

Parameter	Value	Parameter	Value
$\overline{C}_p$	2000 J/kg/K	$\eta\beta'\sigma^*$	0.05
ρ	860 kg/m^3	$E\prime$	222.31 GPa
β	0.0316 C^{-1}	f	0.1
μ at 40 °C	0.0396 Pa.s	H_a	493 MPa
k_{p1}	22 W/m·K	k_{p2}	45 W/m·K

In the first part of the simulations, it is assumed that the rotor rotates in a completely balanced condition with no mass imbalance in the rotor. Therefore, the rotor rotates in its equilibrium position. In this part, the effects of loaded pads wear signatures with different wear severities are explored on the oil film thickness, hydrodynamic pressure distribution, temperature distribution of the oil film and pads, journal eccentricity, and the dynamic coefficients of the system. In the second part of the simulations, an unbalanced rotor is

considered to analyze the dynamic behavior of the system. The effects of the bearing geometrical imperfections on the system nonlinear dynamic behavior and the rub-impact force severity between the rotor and TPJB are also addressed in this part.

This work assumes that two loaded pads experience wear-induced geometrical imperfections and the maximum wear depth occurs on the fifth pad and in front of the pivot. The maximum wear depth on the fourth pad equals half of that of the fifth pad as the fifth pad is closer to the journal equilibrium position when the rotor rotates in the counter-clockwise direction, thus forming more of a severe contact with the journal. The labeling of the pads is shown in Figure 1. The standard deviations of the roughness of both surfaces are equal to 0.4 μm. Intact TPJB and two worn TPJBs with different wear severities are investigated. The effect of wear severity is examined on TPJB thermal and dynamic behavior of the system. The maximum wear depth on the fifth pad of the more severely worn TPJB is assumed to be 20 μm. This TPJB is labeled as the 20 μm worn bearing case in the rest of the paper. The maximum wear depth on the fifth pad of the less severely worn TPJB is equal to 10 μm, and this TPJB is entitled to the 10 μm worn bearing case. The presented model is a simplified model of industrial rotors that operate at high speed and find application in industrial compressors and turbines. The operating speed of this rotor is 10,200 rpm and models for some industrial high speed rotors are presented in [6,8,55,56]. Three speeds of 3500 rpm, the first critical speed of the system, and 10,200 rpm are selected to show the behavior of the system in its equilibrium position. The speed of 3500 rpm represents the system behavior below the first critical speed, while the velocity of 10,200 rpm demonstrates the system behavior in its service operating speed. The oil film thickness and the pressure distribution in the TPJB mid-line are depicted in Figures 3 and 4, respectively. The effects of wear on the loaded pads are visible in the profile of the loaded pads' oil film thicknesses (Figure 3).

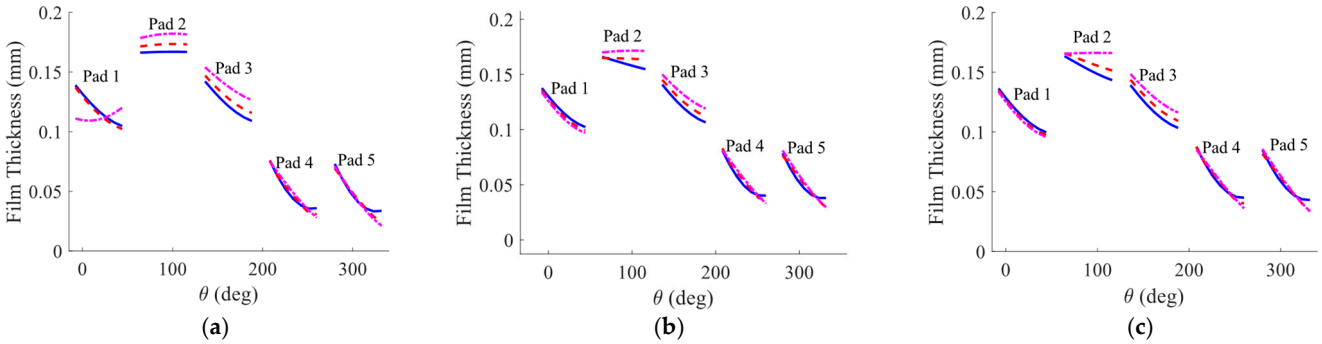

Figure 3. Oil film thickness on intact and worn TPJBs. (**a**) Shaft rotational speed is equal to 3500 rpm (Sommerfeld No: 0.5283, $L/D_b = 0.4$) (**b**) Shaft rotational speed is equal to the first critical speed of the system (Intact bearing Sommerfeld No: 0.7362, 10 μm worn bearing Sommerfeld No: 0.7984, 20 μm worn bearing Sommerfeld No: 0.8562, $L/D_b = 0.4$) (**c**) Shaft rotational speed is equal to 10,200 rpm (Sommerfeld No: 1.0816, $L/D_b = 0.4$). (Blue solid line: Intact bearing, Red dashed line: Bearing with maximum wear depth of 10 μm, Magenta dashed dot line: Bearing with maximum wear depth of 20 μm).

Figure 4a shows the cavitation on the first and the second pads at 3500 rpm when the maximum wear depth is 20 μm. When the system speed reaches its first critical speed, and a worn bearing with 10 μm or 20 μm maximum wear depth is used, cavitation only occurs on the second pad (see Figure 4b). Noteworthy, there is no cavitation on the pads if an intact bearing is used at the first critical speed of the system. Based on Figure 4c, no cavitation can be detected when the operating speed increases to 10,200 rpm and an intact or 10 μm worn TPJB is used; however, cavitation occurs on the second pad when a 20 μm worn TPJB is utilized. The effect of cavitation on the oil film thickness is visible in Figure 3 as well at the mentioned operating conditions. Based on Figures 3 and 4, an increase in the wear depth of the loaded pad leads to an increase in the probability of cavitation on the unloaded pads. Furthermore, the system is more prone to cavitation at lower speeds. The

probability of cavitation formation decreases as the speed increases to the operating speed of the system.

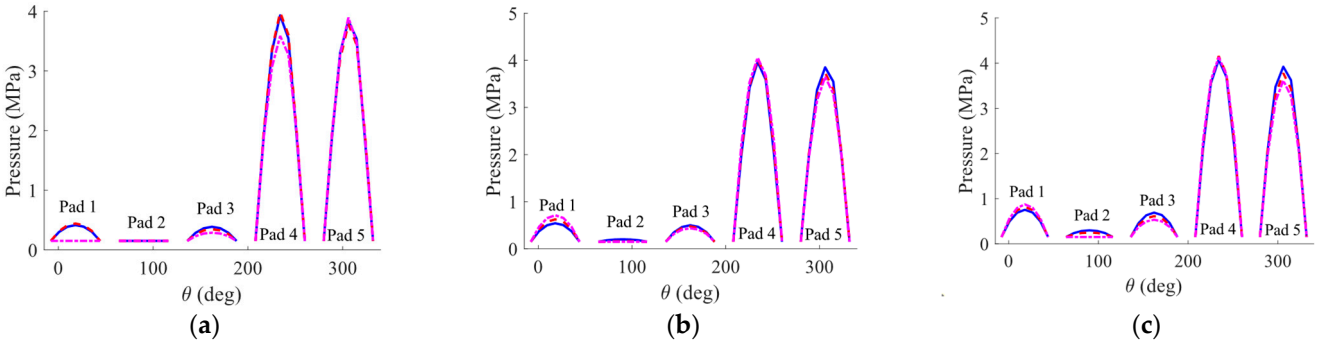

Figure 4. Hydrodynamic pressure distribution on intact and worn TPJBs. (**a**) Shaft rotational speed is equal to 3500 rpm (Sommerfeld No: 0.5283, $L/D_b = 0.4$) (**b**) Shaft rotational speed is equal to the first critical speed of the system (Intact bearing Sommerfeld No: 0.7362, 10 µm worn bearing Sommerfeld No: 0.7984, 20 µm worn bearing Sommerfeld No: 0.8562, $L/D_b = 0.4$) (**c**) Shaft rotational speed is equal to 10,200 rpm (Sommerfeld No: 1.0816, $L/D_b = 0.4$). (Blue solid line: Intact bearing, Red dashed line: Bearing with maximum wear depth of 10 µm, Magenta dashed dot line: Bearing with maximum wear depth of 20 µm).

Figures 5–7 show the effects of intact and worn TPJBs at two different wear severities on the temperature distribution of the pads at 3500 rpm, the system's first critical speed, and 10,200 rpm. Furthermore, Figure 8 presents the inner surface temperature of the pads at 3500 rpm, the first critical speed of the system, and 10,200 rpm. Based on Figures 5–7, the wear in loaded pads decremented the temperature in the unloaded pads while raising the temperature increase in the loaded ones. This temperature change is due to a shift in the journal equilibrium position towards a location closer to the loaded pads when a worn TPJB is used. Furthermore, the wear-induced temperature variations of the pad are more severe at lower speeds. Considering Figure 8, the fifth pad, which experiences more severe wear, has a higher temperature variation near its trailing edge. This is because the lubricant enters the space between the pad and the journal from the pad's leading edge at a lower temperature. The pad and the lubricant's temperature increase along the pad's arc length, but the pad's temperature slightly decreases due to convection heat transfer at its trailing edge. Therefore, the maximum temperature in loaded pads will be near the pads' trailing edge but not exactly on the trailing edge. The point near the trailing edge of the loaded pads is a good location for monitoring pad temperature and detecting TPJB wear at an early stage because of the high temperature variation at this point. The temperature variations of the loaded pads near their trailing edges provide an accurate indicator to determine the wear severity and bearing geometrical imperfections. This phenomenon was described by Lee et al. [2] to diagnose wear in TPJB using an experimental test-rig as well.

The effects of using intact and worn TPJBs on the temperature variations of the loaded pads near their trailing edges are shown in Figure 9a,b for a range of shaft rotational speeds. The temperature of a point on the pad surface at the distance of 71% of the arc length of the pad from its leading edge is shown in these figures. This point on loaded pads is appropriate for temperature measurement using probes in experimental and industrial studies as it is near the trailing edge of the pad and experiences more temperature variations due to wear. It should be noted that the fifth pad temperature rises more significantly than the fourth pad because the fifth pad is closer to the journal equilibrium position in this simulation. Furthermore, the wear-induced pad temperature rise is more significant at low speeds and slightly decreases by increasing the shaft speed since the rotor rotates closer to the loaded pads at lower speeds. Based on the results, it is recommended to measure the temperature of the loaded pads near their trailing edges at lower speeds in a balanced rotor-TPJB system to detect the bearing wear. The effect of wear of the loaded pads on the

journal eccentricity is also illustrated in Figure 9c. As seen, an increase in the wear depth of the pads raises the journal eccentricity. Figure 9d shows the equilibrium locus of the pad's tilt angle versus the maximum pressure on each pad for shaft speeds ranging from 3500 rpm to 11,000 rpm. According to this figure, the tilt angle of the fifth pad exhibits less variation compared to the other pads in the given speed range. Additionally, pad No. 2 experiences the least variation in applied maximum pressure since it is the unloaded pad.

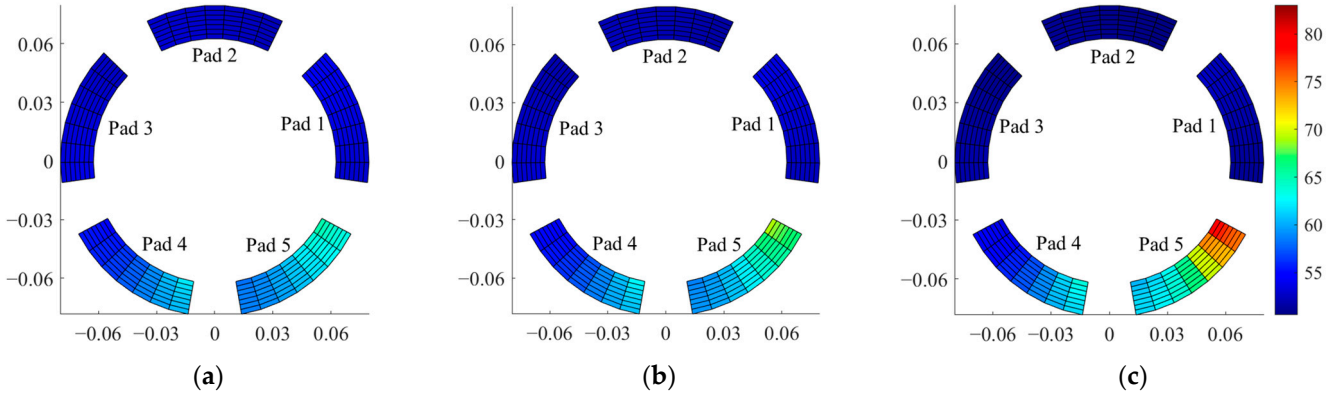

Figure 5. Pad temperature distribution at 3500 rpm. (**a**) Intact bearing (**b**) Maximum wear depth: 10 µm (**c**) Maximum wear depth: 20 µm (Sommerfeld No: 0.5283, $L/D_b = 0.4$, Axes unit: meter).

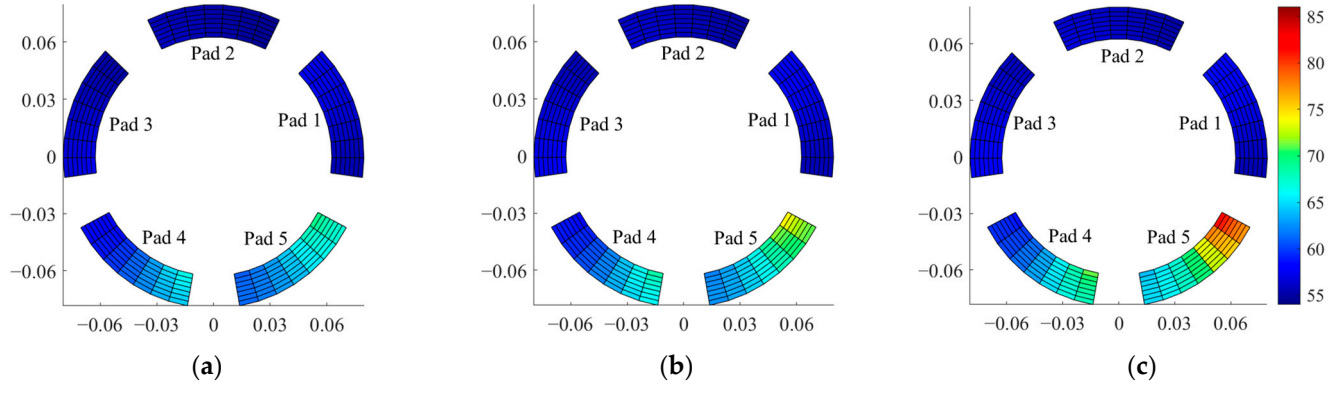

Figure 6. Pad temperature distribution at the first critical speed of the system. (**a**) Intact bearing (**b**) Maximum wear depth: 10 µm (**c**) Maximum wear depth: 20 µm (Intact bearing Sommerfeld No: 0.7362, 10 µm worn bearing Sommerfeld No: 0.7984, 20 µm worn bearing Sommerfeld No: 0.8562, $L/D_b = 0.4$, Axes unit: meter).

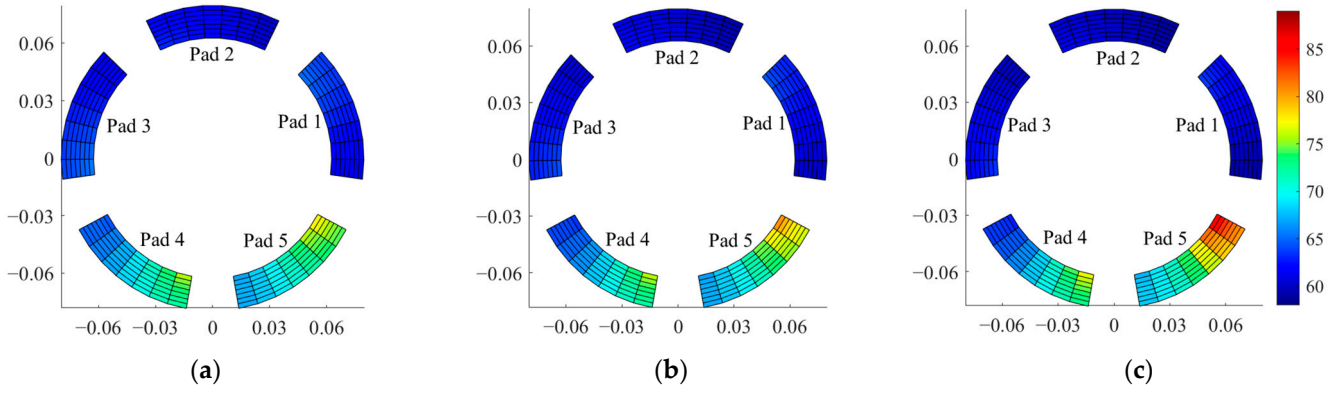

Figure 7. Pad temperature distribution at 10,200 rpm. (**a**) Intact bearing (**b**) Maximum wear depth: 10 µm (**c**) Maximum wear depth: 20 µm (Sommerfeld No: 1.0816, $L/D_b = 0.4$, Axes unit: meter).

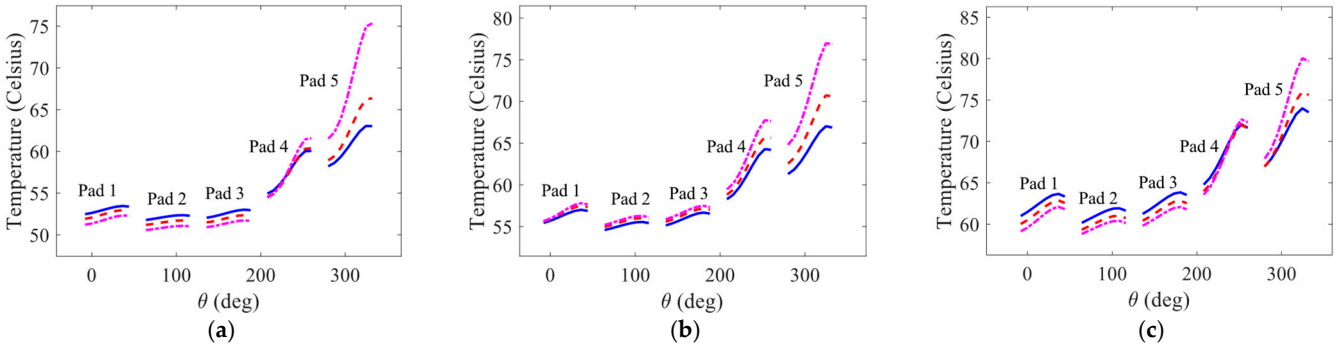

Figure 8. Pads inner surface temperature for intact and worn TPJBs (**a**) Shaft rotational speed is equal to 3500 rpm (Sommerfeld No: 0.5283, $L/D_b = 0.4$) (**b**) Shaft rotational speed is equal to the first critical speed of the system (Intact bearing Sommerfeld No: 0.7362, 10 µm worn bearing Sommerfeld No: 0.7984, 20 µm worn bearing Sommerfeld No: 0.8562, $L/D_b = 0.4$) (**c**) Shaft rotational speed is equal to 10,200 rpm (Sommerfeld No: 1.0816, $L/D_b = 0.4$). (Blue solid line: Intact bearing, Red dashed line: Bearing with maximum wear depth of 10 µm, Magenta dashed dot line: Bearing with maximum wear depth of 20 µm).

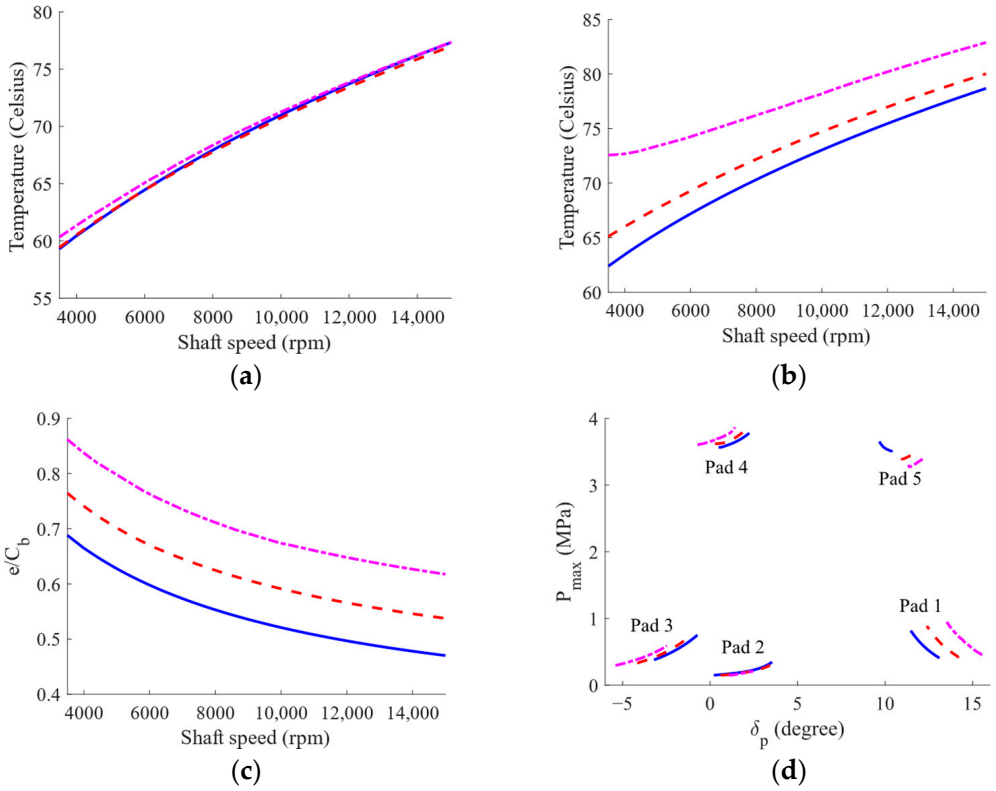

Figure 9. The effect of wear in loaded pads considering variable shaft speed (**a**) Pad number 4 temperature in 71% of the pad's arc length from its leading-edge (**b**) Pad number 5 temperature in 71% of the pad's arc length from its leading-edge. (**c**) Journal eccentricity (**d**) Equilibrium locus of the pads tilt angle versus the maximum pressure on pads for the shaft speed of 3500 rpm to 11,000 rpm (Blue solid line: Intact bearing, Red dashed line: Bearing with maximum wear depth of 10 µm, Magenta dashed dot line: Bearing with maximum wear depth of 20 µm).

It is worth mentioning that the variations in the lubricant temperature will change the lubricant viscosity, which affects the dynamic coefficients of the system. Here, the TPJB dynamic coefficients are obtained considering the geometrical imperfections of the pads based on the procedure presented in [57]. The perturbed Reynolds equation is solved to

obtain the perturbed oil film thickness and pressure, which are then used to calculate the bearing linear dynamic coefficients. These dynamic coefficients are then reduced to the shaft degrees of freedom using the procedure presented in [4]. Figures 10 and 11 shows the changes in the dynamic coefficients of the intact and worn bearings versus the shaft rotating speeds. Accordingly, the dynamic coefficients of the bearing show less sensitivity to geometrical imperfections at higher speeds. This phenomenon can be assigned to the formation of a thicker oil film at higher shaft speed, therefore, the rotor rotates farther than the loaded pads.

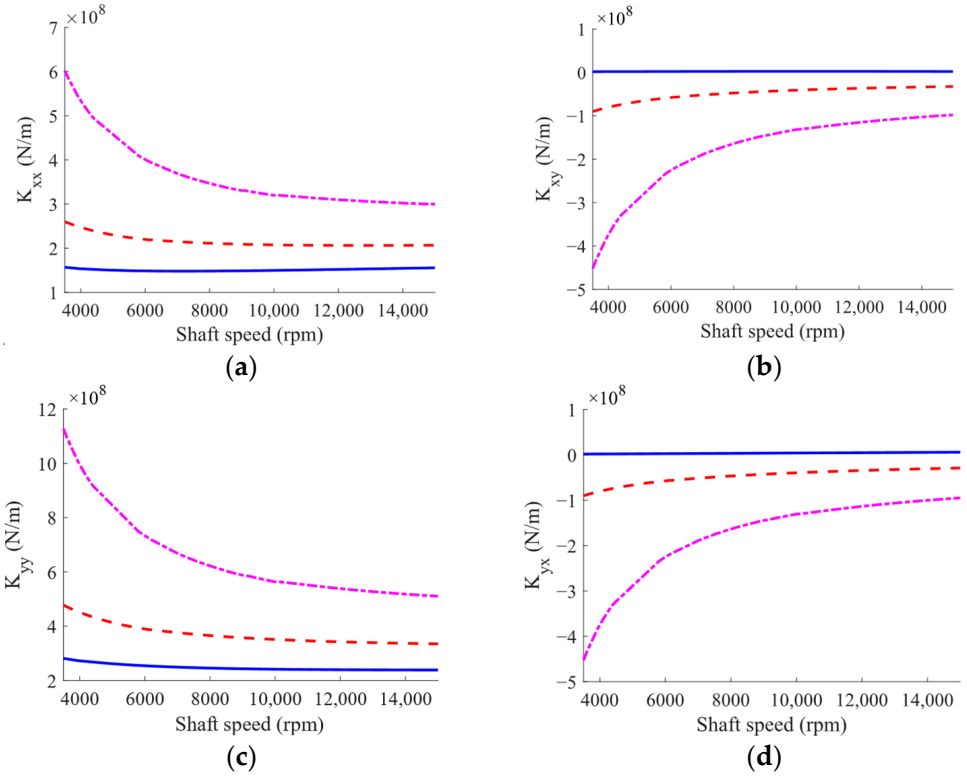

Figure 10. TPJB stiffness for intact and worn bearings cases at different speeds (**a**) K_{xx} (**b**) K_{xy} (**c**) K_{yy} (**d**) K_{yx} (Blue solid line: Intact bearing, Red dashed line: Bearing with maximum wear depth of 10 µm, Magenta dashed dot line: Bearing with maximum wear depth of 20 µm).

Furthermore, an increase in the wear severity leads to the creation of the cross-coupling terms of the TPJB stiffness and damping coefficients which can affect the system stability. To investigate the stability of the proposed model, the eigenvalue problem is solved at the equilibrium state of the system. The results show that all eigenvalues have negative real parts, indicating that the system is stable at its equilibrium position for shaft rotational speeds ranging from 3500 rpm to 11,000 rpm, regardless of whether the bearing is intact or suffered from wear with a maximum depth of up to 20 µm. A detailed description of linear stability analysis for TPJBs is provided in [58]. However, an increase in the sleeve bearing wear severity can lead to decrease in bearing stiffness [59], according to Figures 10 and 11, the increase in the wear severity in TPJBs with load between pads (LBP) configuration results in an increase in direct dynamic coefficients due to the enhancement of the wear-induced asymmetry and preload of the TPJBs. The increase in TPJBs dynamic coefficients with LBP configuration due to the bearing preload and bearing asymmetry enhancement was also discussed in [5,60,61].

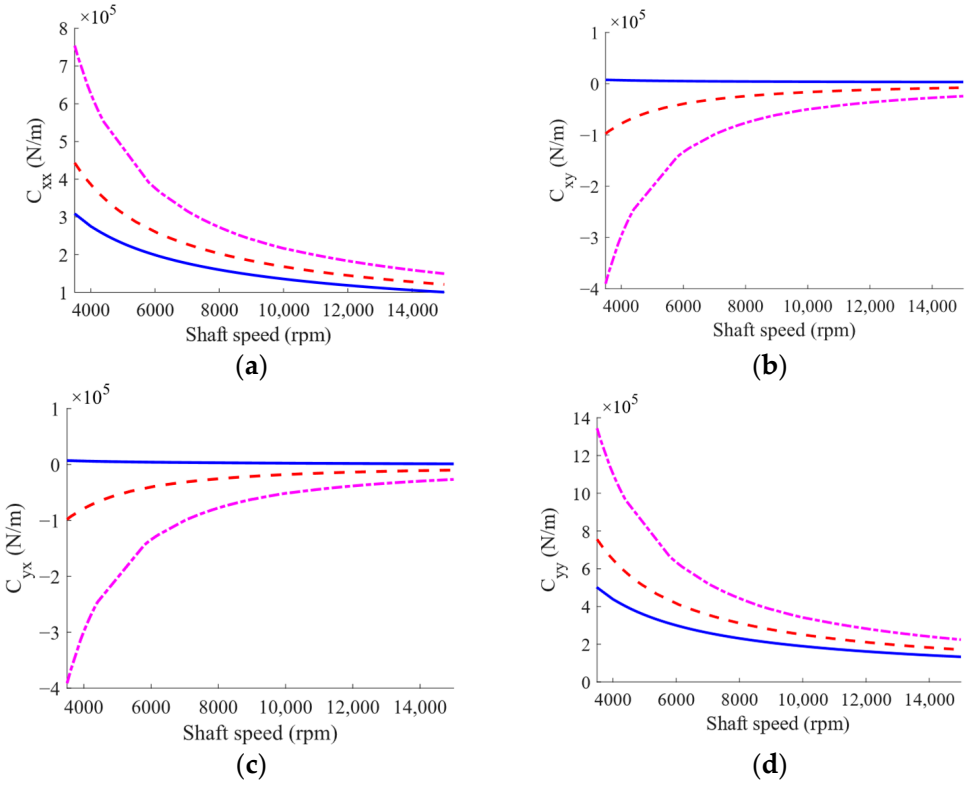

Figure 11. TPJB damping for intact and worn bearings cases at different speeds (**a**) C_{xx} (**b**) C_{xy} (**c**) C_{yx} (**d**) C_{yy} (Blue solid line: Intact bearing, Red dashed line: Bearing with maximum wear depth of 10 µm, Magenta dashed dot line: Bearing with maximum wear depth of 20 µm).

In the proposed model, flexible rotor vibration amplitudes are obtained at the disc and the journal locations using the calculated dynamic coefficients as shown in Figure 12. This figure shows that the high damping of the TPJB results in the creation of a flat peak. It can be observed that an increase in the wear depth of the TPJB with the LBP configuration reduces its ability to suppress high vibration levels when passing through the system's critical speed. Moreover, an increase in the wear severity of loaded pads of TPJB with LBP configuration, increases the vibration amplitude of the rotor at its mid-point at the critical speed of the system. The first critical speed of the rotor-bearing system increases due to the increase in the asymmetry of the worn TPJB and the subsequent increase in the TPJB stiffness. Therefore, the increase in wear on loaded pads causes a shift in the first critical speed of the system. Changes in the first critical speed of the system and the rotor vibration amplitude induced by the bearing wear are quantitatively shown in Table 4. According to this table, the system's first critical speed value and its vibration amplitude are good indicators of wear severity in TPJBs at its early stages.

Table 4. The effect of the bearing wear severity on the rotor-TPJB first critical speed and the variation of the rotor's vibration amplitude.

Maximum Wear Depth	First Critical Speed	Increase in Vibration Amplitude of the Journal	Increase in Vibration Amplitude of the Disc
Intact bearing	5500 rpm	-	-
10µm	6200 rpm	23.7%	47.2%
20µm	6900 rpm	52.6%	253.3%

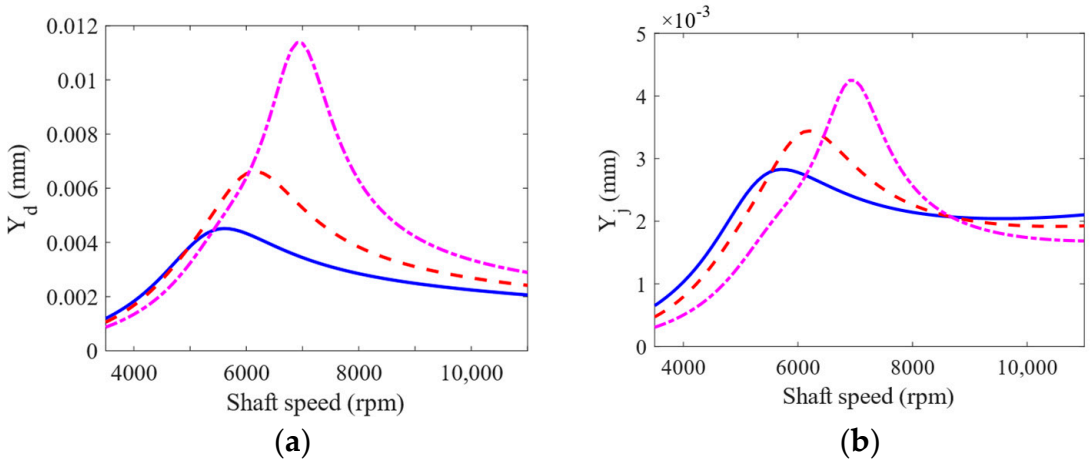

Figure 12. Rotor vibration amplitudes for intact and worn TPJBs considering 2×10^{-6} kg·m mass unbalance on disc (**a**) Disc vibration amplitude (**b**) Journal vibration amplitude (Blue solid line: Intact bearing, Red dashed line: Bearing with maximum wear depth of 10 μm, Magenta dashed dot line: Bearing with maximum wear depth of 20 μm).

In the next part of the paper, it is assumed that the disc has a 0.04 kg·m unbalanced mass. Therefore, the rotor orbits around its equilibrium position at the steady state. In such conditions, the contact between the journal and the bearing is possible due to the high vibration level of the rotor, possibility of fluttering of unloaded pads, and the wear-induced geometrical imperfections of the loaded pads. It is worth mentioning that, however, the system operates in laminar condition in its equilibrium state, the oil film flow can convert to turbulent flow at high speeds and high vibration amplitudes. Therefore, the generalized Reynolds equation is used to calculate the oil film pressure distribution. Figures 13 and 14 show the solid-to-solid contact pressure induced by the rub-impact between the journal and the pads at different speeds and bifurcation diagrams for the journal center in horizontal and vertical directions. The bifurcation diagrams are produced by plotting the data from the journal vibration signal versus shaft rotational speed. The data from the vibration signal must have a sampling rate of one period, and these diagrams show the periodic and non-periodic motion of the journal at different levels of wear severity. Based on Figure 14, the rotor motion is period one for the intact bearing at the speeds of 3500–7500 rpm and Figure 13, shows no contact between the journal and the pads for intact bearing case in the mentioned speed range. According to Figure 13, contact occurs between the unbalanced rotor and the 2nd pad when there is a wear signature on the loaded pads with a maximum wear depth of 10 μm in the shaft speed range of 5250–5500 rpm. Since the 2nd pad is unloaded, the contact occurs due to pad flutter. Moreover, the rotor motion changes to irregular patterns at the mentioned speed range and then returns to period one based on Figure 14. The effect of pad fluttering on a rotor-TPJB dynamic behavior and the rotor irregular motion induced by pad fluttering was studied in previous works [62] using bifurcation diagrams.

When wear depth increases to 20 μm, contact between the journal and the 5th pad of the bearing starts from 4500 rpm and increases with the rotor speed until reaching its maximum severity at 5250 rpm. Contact pressure decreases beyond this speed, and vanishes at 6000 rpm. The fifth pad is a loaded pad and the mentioned journal-bearing contact is induced by the wear signature on this pad. For this case, Figure 14 shows irregular rotor motion in the speed range of 5250 to 5750 rpm where the obtained vibration amplitude is larger than the 10 μm worn bearing case at the same speed range. Based on Figure 13, the contact between the journal and the unloaded pad vanishes when the maximum wear depth increases to 20 μm; but contact between the journal and the loaded pad becomes more severe than the 10 μm worn bearing case. Since an increase in loaded pad wear depth changes the journal orbit location to a lower position in the bearing, the increase in the

bearing wear severity decreases the probability of contact between the journal and upper pads while increasing the rub-impact between the journal and the lower pads.

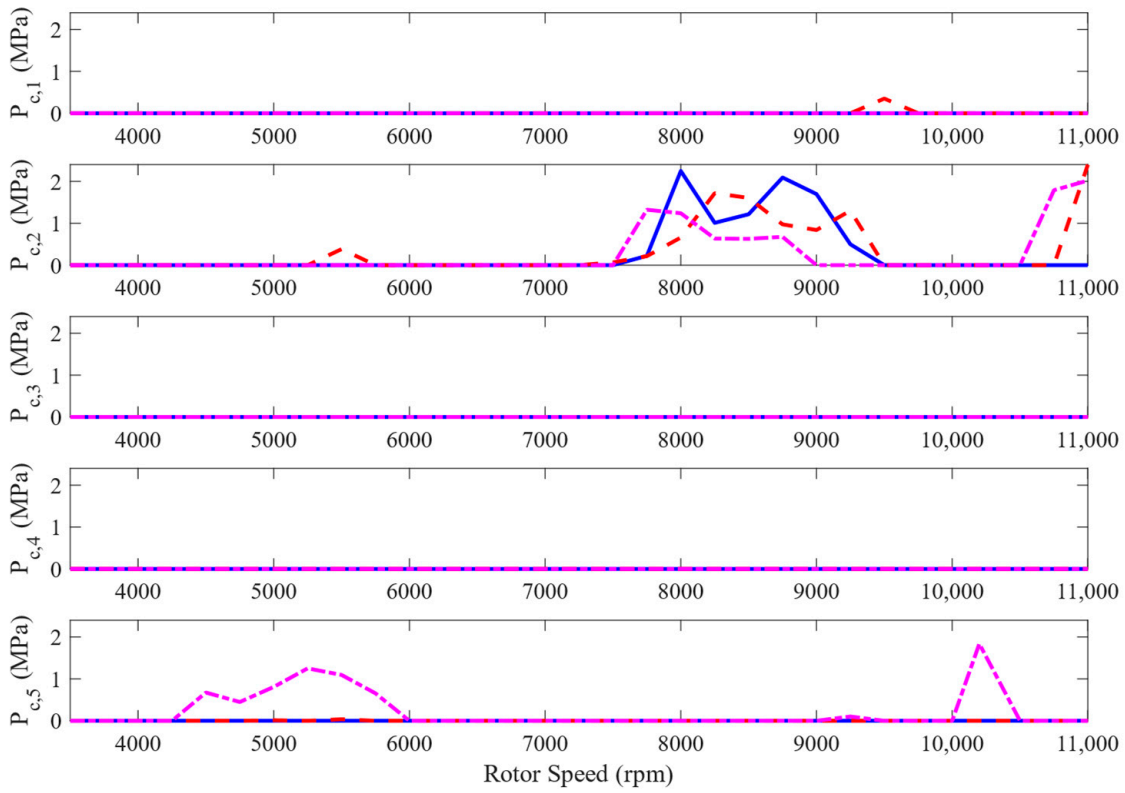

Figure 13. Solid-to-solid contact pressure induced by journal-bearing contact at different speeds for pad No. 1 to pad No. 5 in the intact and worn bearing cases (Blue solid line: Intact bearing, Red dashed line: Bearing with maximum wear depth of 10 μm, Magenta dashed dot line: Bearing with maximum wear depth of 20 μm).

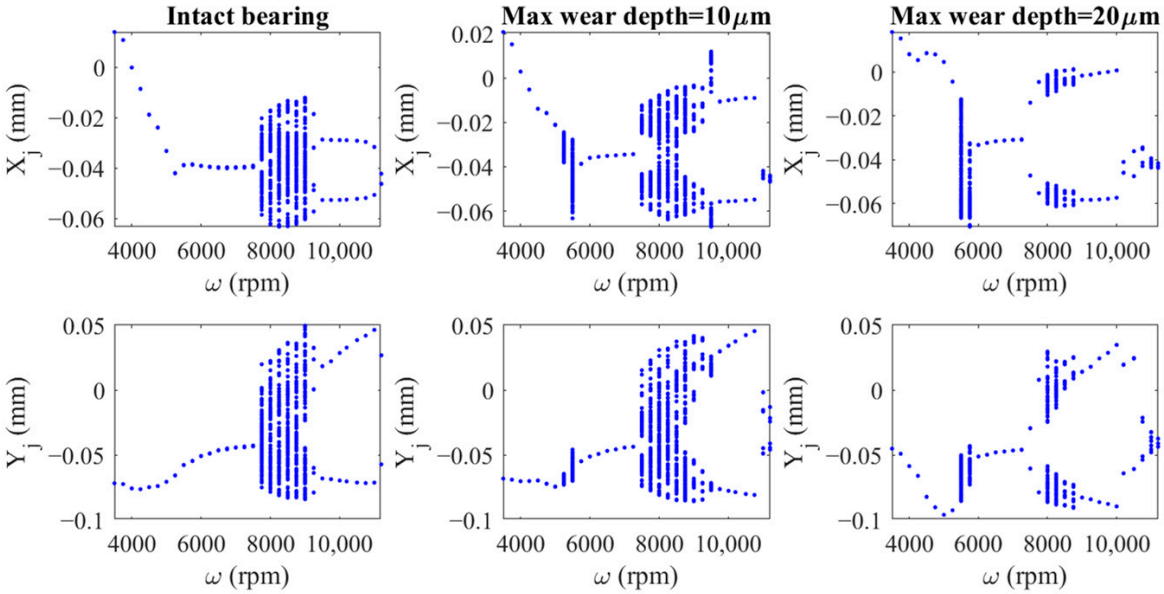

Figure 14. The journal displacement bifurcation diagrams in different speeds for the intact and the worn bearing cases.

As shown in Figure 12, the increase in vibration amplitude in the mentioned speed range is due to the first critical speed of the rotor. In this situation, the rotor rotates near the bearing due to its low speed, and journal-bearing contact is arisen from its high mass unbalance. These observations conclude that the increase in wear depth in loaded pads makes the rotor-bearing system more prone to experiencing an increase in wear and rub-impact near the first critical speed of the system.

By enhancing the rotor speed, the rotor rotates nearer to the bearing center and the oil film forms to separate the journal and the bearing. Based on Figure 13, there will be no contact between the journal and the bearing in the speed range of 5750–7500 rpm for an intact and a 10 μm worn bearing case. For the 20 μm worn bearing case, no contact is expected in the speed range of 6000 to 7500 rpm. The period one motion of the rotor is visible from Figure 14 for the speed range of 5750–7500 rpm. Journal-bearing contact starts again at 7500 rpm for all intact and worn bearing cases. According to Figure 13, this contact occurs between the journal and the second pad which is an unloaded pad. This phenomenon is due to the high mass imbalance of the rotor and the unloaded pad flutter.

Figure 13 also suggests that the rotor experiences a lower contact pressure between the journal and the upper pad during pad fluttering in the mentioned speed range as the wear depth on loaded pads increases. Such a trend can be assigned to the lower orbit position of rotor in a worn TPJB, which decreases the contact between the journal and the upper pads. Figures 13 and 14 show that the rotor motion changes to period two and the contact pressure vanishes at higher speeds.

Figure 13 shows that the rotor-intact TPJB operates without journal-bearing contact in the speed range of 7500–11,000 rpm, suggesting that the unbalanced rotor-intact TPJB can work without rub-impact at its service speed (10,200 rpm). The journal-worn bearing contact starts again at 10,200 rpm for the 20 μm worn bearing case which is induced by the contact between the journal and the 5th pad (see Figure 13). Furthermore, the contact between journal and the upper pad appears again at 10,500 and 10,750 rpm for the 10 μm worn bearing and the 20 μm worn bearing cases, respectively. Based on Figures 13 and 14, the journal-intact bearing has much better dynamic behavior than a worn TPJB at 10,200 rpm (the standard operating speed of the system). Furthermore, an increment in wear of the loaded pads increases the journal-bearing rub-impact and promotes the irregular dynamic motion around the service speed of the system.

Waterfall diagrams for the intact and the worn bearing cases are illustrated in Figure 15a–c. The effects of oil whirl which is induced by the oil film nonlinear force [63] are recognizable in these diagrams. Note that the frequency of the oil whirl equals half of the rotational frequency of the journal. Moreover, the oil whip has a constant frequency that approximately equals the first critical speed of the system [64]. The effects of oil whirl and oil whip are observed in waterfall diagrams. Therefore, when the system is subjected to high mass unbalance loads and in certain speed ranges, the system exhibits non-periodic behavior and large shaft vibration amplitudes due to the impact of the oil film, as well as the rub-impact force. The zoomed plots in Figure 15a–c present the speeds at which the oil whirl effect starts to appear in the system frequency response. The velocity signal amplitude is also depicted for 1X and 5X frequency component at the shaft speed of 3500 rpm. Based on Figure 15a, the oil whirl starts at 8000 rpm, and its amplitude increases at 9000 rpm for the case of the intact bearing. For both 10 μm and 20 μm worn bearing cases, oil whirl effects appear sooner at 7500 rpm (Figure 15b,c). Therefore, the minor wear in loaded pads of the TPJB with LBP configuration can lead to the oil whirl at a slightly lower speed compared to the intact TPJBs.

Since the rotor rotates closer to the loaded pads at the lower speeds, the signals of the system motion at low speeds can better show the effects of the geometrical imperfections of the hydrodynamic bearing [24]. Therefore, the peak amplitudes of the velocity signal are investigated at three speeds of 3500 rpm, the first critical speed of the system, and 10,200 rpm. It is worth mentioning that 3500 rpm represents one of the sub-critical speeds, while the operating speed of the system is 10,200 rpm. The mentioned values are chosen

for the shaft speed to compare the intact and worn TPJB velocity signal peak amplitudes to analyze the effects of the geometrical imperfections of the loaded pads on the dynamic motion of the system.

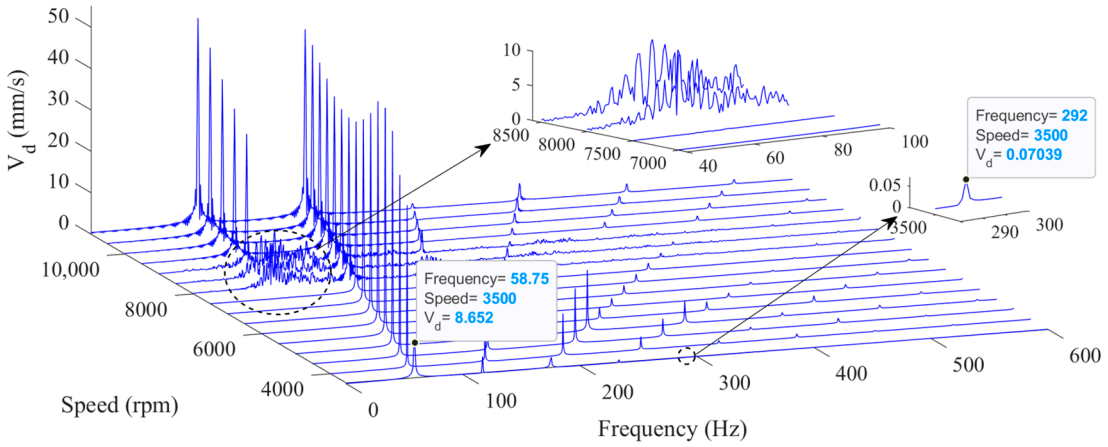

(**a**)

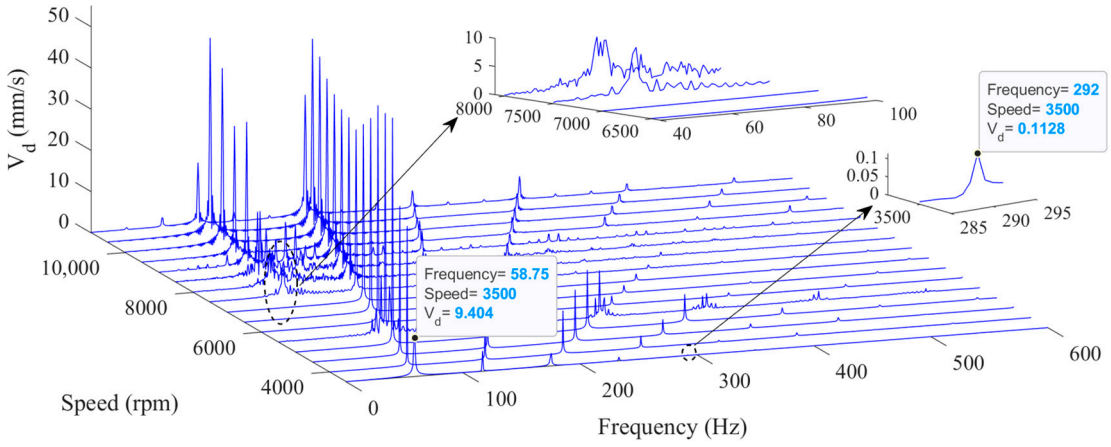

(**b**)

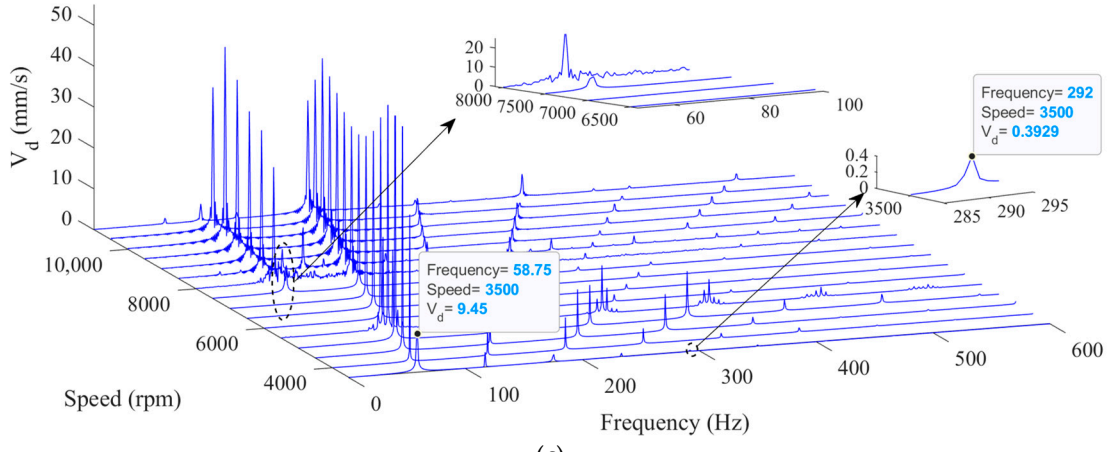

(**c**)

Figure 15. Waterfall diagrams for disc velocity in a range of rotor speeds and different wear severities, (**a**) Intact bearing (**b**) Maximum wear depth: 10 µm (**c**) Maximum wear depth: 20 µm.

Table 5 lists the amplitudes of the disc velocity signal peaks at 3500 rpm. Furthermore, the peak amplitudes of 1X and 5X frequency components are depicted in Figure 15a–c for the mentioned signals. According to Figure 15a–c and Table 5, an increase in maximum wear depth of the bearing enhances the 1X harmonic component of the velocity signal. Moreover, the increase in wear depth increments in the disc velocity signals of the 5X, 6X, and 7X components. The experimental observations in [37] also show similar behavior for the frequency response of a worn TPJB velocity signal at low speeds. Therefore, 1X, 5X, and higher harmonic components of the shaft velocity signal at low speeds provide an accurate indicator for detecting the wear severity of the bearing at its early stages.

Table 5. Peak amplitudes of the disc velocity signal spectra at 3500 rpm in mm/s.

	1X	2X	3X	4X	5X	6X	7X
Intact bearing	8.652	4.064	2.604	0.7275	0.07039	0.09018	0.01463
10 μm wear depth	9.404	4.955	3.166	0.9615	0.1128	0.1643	0.02591
20 μm wear depth	9.45	3.683	1.88	0.917	0.3929	0.3704	0.0915

Tables 6 and 7 show the amplitude of the disc velocity signal at the first critical speed of the system and 10,200 rpm (i.e., operating speed of the system). Furthermore, the TPJB system experiences the oil whirl at 10,200 rpm. The whirl amplitudes at 0.5X frequency components are shown in Table 7. Since an increase in the shaft speed shifts the journal equilibrium position toward the bearing center, the journal rotates in a farther place relative to the worn pads at higher speeds. Therefore, the geometrical imperfections of the bearing have a more negligible effect on the dynamics of the system, and the peak amplitudes of the velocity signal cannot be used for wear detection at this speed.

Table 6. Peak amplitudes of the disc velocity signal spectra at the first critical speed of the system in mm/s.

	1X	2X	3X	4X	5X	6X	7X
Intact bearing	52.04	8.922	14.81	5.486	0.8825	0.8505	0.3522
10 μm wear depth	53.55	8.032	11.41	3.837	1.534	0.3031	0.2553
20 μm wear depth	62.89	6.998	11.78	6.383	2.414	1.044	0.4888

Table 7. Peak amplitudes of the disc velocity signal spectra at 10,200 rpm in mm/s.

	0.5X	1X	1.5X	2X	2.5X	3X	3.5X
Intact bearing	42.43	43.23	2.685	3.005	1.56	1.338	0.503
10 μm wear depth	44.77	44.59	2.972	3.788	2.232	1.568	0.8926
20 μm wear depth	34.39	35.3	4.073	0.9427	1.785	1.68	0.9641

The effects of wear-induced geometrical imperfections of the bearing on the variations of the velocity signal peak amplitudes are shown in Table 8 at 3500 rpm and the first critical speed of the system. According to this table, the velocity signals of 1X and 5X harmonic components are good indicators to detect wear in the loaded part of the TPJB.

Table 8. Effect of wear severity on disc vibration amplitude at 3500 rpm and the first critical speed.

Maximum Wear Depth	Rotor Speed	Increase in 1X Vibration Amplitude	Increase in 5X Vibration Amplitude
10 μm	3500 rpm	8.6%	160%
	First critical speed (6200 rpm)	2.9%	73%
20 μm	3500 rpm	9.2%	558%
	First critical speed (6900 rpm)	20.8%	273%

Table 9 presents the journal center orbit diagrams at 3500, 5500, 10200, and 11,000 rpm. These results are shown for the intact and two worn bearing cases with a maximum wear depth of 10 µm and 20 µm, respectively. According to Figure 12, the 5500 rpm is the first critical speed of the rotor-intact TPJB system. Furthermore, the standard operating speed of the system equals to 10,200, hence, the speed of 11,000 rpm exceeds the standard operating speed of the system. Based on Table 9, the wear in loaded pads changes the periodic motion of the rotor to irregular motion. Furthermore, TPJB keeps its period two motion at 10,200 rpm when a bearing with 10 µm maximum wear depth is used. But if the maximum wear depth increases to 20 µm, the system behavior changes to the irregular motion. It is worth mentioning that 10 µm wear depth changes the system behavior from period two to period six motion at the speed of 11,000 rpm.

Table 9. Journal orbits in selected rotational speeds for intact and worn bearing cases.

	3500 rpm	**5500 rpm**	**10,200 rpm**	**11,000 rpm**
Intact bearing	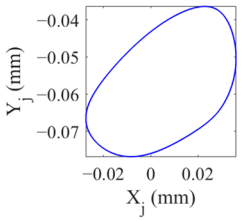	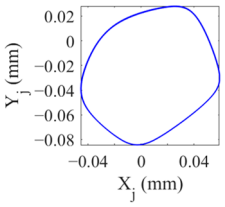	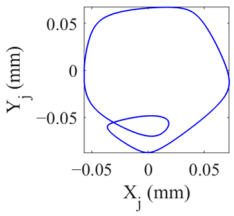	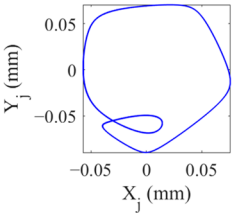
$d_{max,5} = 10$ µm	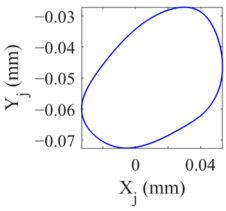	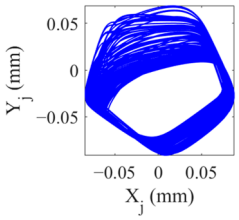	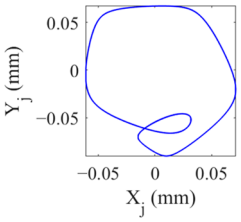	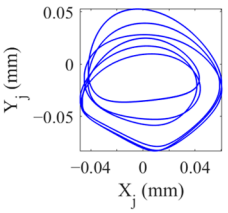
$d_{max,5} = 20$ µm	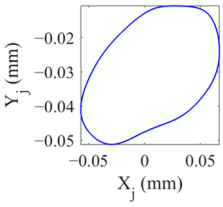	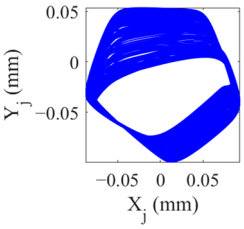	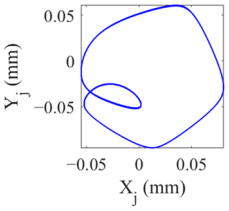	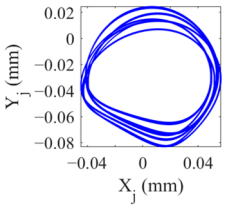

To sum up, the increase in the wear severity of the bearing is detectable by analyzing the dynamic behavior of the system as well as the temperature trend of the pads. This paper shows that the temperature of the loaded pads near their trailing edges and 1X, 5X, and higher harmonic components of the disc velocity signal are suitable indicators for detecting TPJBs wear severity at the early stages. Furthermore, wear on the loaded pads negatively affects the dynamic behavior of the system at low, middle, and standard operating speeds.

4. Conclusions

This paper presents a novel tribo-dynamic model for a flexible rotor-tilting pad journal bearing (TPJB) which integrated the geometrical imperfections of the bearing and journal-bearing rub-impact in one model. This model is used to study the effects of the minor wear-induced geometrical imperfections on the dynamic behavior of the system. Furthermore, the effects of the geometric imperfections of the TPJB with load between pads (LBP) configuration on the rub-impact severity between the journal and the bearing was also investigated. Mixed lubrication theory was used to simulate the contact between the journal and the bearing and the Reynolds equation was solved via the finite element method to determine the oil film hydrodynamic pressure distribution on pads. Energy and heat

equations were solved to obtain the temperature distribution of the oil film and pads. The effects of using worn TPJBs on the journal equilibrium position, pads temperatures, contact pressure between journal and bearing, and the dynamic behavior of the system were studied for different speeds. The simulations revealed that the geometrical imperfections of the worn bearing increase the journal eccentricity and the temperature of the loaded pads near their trailing edges. Hence, the variations in the system equilibrium state provide a useful indicator for monitoring the bearing wear at its early stages. The effects of the bearing wear were more visible at low shaft speeds. It is worth mentioning that the wear-induced clearance variations of the pads alter the dynamic coefficients of the bearing and change the critical speed of the system.

The nonlinear dynamic behavior of an unbalanced rotor-worn TPJB was studied using the present model. The journal orbit plots, contact pressure, and bifurcation diagrams were obtained by the mentioned simulation which showed that the wear-induced geometrical imperfections of the bearing can lead to irregular motion in the system, increase the possibility of unloaded pads flutter in some speeds and more damaging behavior due to journal-bearing contact. These observations show the necessity of wear detection at its early stages to prevent more catastrophic failures. On the other hand, the analysis of the vibration harmonic components from the spectral analysis of the disc velocity signal showed that the utilization of the worn TPJB with LBP configuration can trigger oil whirl at slightly lower speeds. Furthermore, the amplitudes of the velocity signals of the 1X, 5X, 6X, and 7X harmonic components of the rotor-worn TPJB increased at sub-critical speeds by enhancement of the wear severity. Therefore, an analysis of the velocity signal of the system at low speeds provided an appropriate indicator to detect the wear-induced geometrical imperfections of the bearing.

The results of this work can be used for simulation, online condition monitoring, and fault diagnosis purposes for TPJBs to show and detect the effects of bearing wear and journal-bearing rub-impact on the behavior of the system.

Author Contributions: Conceptualization, E.T.-N. and M.S.S.; methodology, E.T.-N.; software, E.T.-N.; validation, E.T.-N.; formal analysis, E.T.-N.; investigation, E.T.-N.; resources, E.T.-N. and M.S.S.; writing—original draft preparation, E.T.-N.; writing—review and editing, E.T.-N. and M.S.S.; visualization, E.T.-N.; supervision, M.S.S.; project administration, M.S.S. All authors have read and agreed to the published version of the manuscript.

Funding: This research received no external funding.

Data Availability Statement: Not applicable.

Acknowledgments: The authors appreciate the late Hamid Ahmadian who passed away on August 2021, for his comments and suggestions for this work.

Conflicts of Interest: The authors declare no conflict of interest.

Nomenclature

$\overline{C}_P$	Oil specific heat capacity
C_b	Bearing clearance
D_s, D_b, D_j, D_p	Diameters of shaft, bearing, journal, and pads
$d_{w,p}, d_{max,p}$	Local and maximum wear depth on the p'th pad
E', E_s	Equivalent and shaft young modulus
e	Journal eccentricity
f	The friction coefficient between journal and pads
f_p	The fractional rotational position of the pivot
H_a	The hardness of the softer material
J_p	Moment of inertia of p'th pad

k_{p1}, k_{p2}, k_{p3}	Conduction coefficient on pad inner surface, outer surface, and edges
L, L_j, L_s, L_g	Lengths of bearing, journal, shaft and groove
m_d, m_j	Masses of disc and journal
m	Preload
N_{pad}	Number of pads
$P_{sup}, Q_{sup}, T_{sup}$	Supply pressure, oil flow, and pressure
t_d, t_p	Thicknesses of disc and pads
W_b	Bearing load
$\alpha_{s,p}, \alpha_{e,p}$	Starting and ending angle of wear on the p'th pad
β	Thermo-viscosity index
$\beta\prime$	Mean radius of asperities
δ_p, Δ_p	Tilt angle and pad arc angle of the p'th pad
η	Asperity density
$\theta_p, \theta_{s,p}, \theta_{e,p}$	Pivot, leading and trailing angles of the p'th pad
μ, μ_0	Oil viscosities at T and T_0
σ_1, σ_2	Asperity height standard deviations of pads and journal
ν	Poisson ratio
ρ, ρ_s	Densities of the Oil and shaft
ω	The rotational speed of the rotor

Appendix A

The tilting pad journal bearing (TPJB) model presented in this work considers the effect of wear, oil film viscosity variations with temperature, oil film turbulence and journal-bearing contact on the dynamic behavior of a flexible rotor-TPJB model. To verify the proposed model for TPJB, the dynamic coefficients of the TPJB are obtained using the proposed model and the results are compared by previous experimental findings and numerical results which presented by Dmochowski and Brockwell [65]. The specifications of this system are given in Table A1, and the results are shown in Figure A1. It is seen that the proposed model predicts the TPJB dynamic coefficients more accurately than the presented results in [65].

The proposed model is also verified for worn bearings by comparing the modeled results with a previous study for a journal-sleeve worn bearing system with a rough surface [26], whose properties are presented in Table A2. This research is considered to verify the journal bearing contact pressure distribution, hydrodynamic pressure distribution, and wear profile in the bearing. Oil is supplied to this bearing via a groove located at the top. Further details of this model can be found in [26].

The contact and hydrodynamic forces for the mentioned sleeve bearing are obtained using the proposed bearing model which is then verified with the presented numerical results in [26] as shown in Figure A2. Hydrodynamic and contact pressure distributions at the mid-line of the worn bearing are depicted in Figure A2 where P denotes pressure and θ shows the bearing circumferential direction.

Table A1. Tilting pad journal bearing properties presented in [65].

Parameter	Value	Parameter	Value
L	0.057 m	f_p	0.5
D_j	0.076 m	ρ	850 kg/m^3
t_p	0.016 m	$\overline{C_p}$	2200 J/kg·K
D_b	0.07612 m	k_{p1}	0.15 W/m·C
W_b	4000 N	k_{p2}	45 W/m·C
m	0	μ_1 at $T_1 = 38$ °C	0.027 Pa·s
Δ_p	54°	μ_2 at $T_2 = 99$ °C	0.005 Pa·s
Q_{sup}	7×10^{-5} m^3/s	T_{sup}	50 °C

Table A2. Journal-plain bearing properties presented in [26].

Parameter	Value	Parameter	Value
$\left(D_b - D_j\right)/D_b$	0.001	E'	83.6 GPa
L/D_b	0.5	H_a	250 MPa
L_g/L	0.8	P_{sup}	0.1 MPa
D_b	100 mm	β'	0.05 mm
W_b	10 kN	$\eta\beta'\sigma^*$	0.05
θ_g	$\pi/9rad$	μ	0.0272 Pa·s
ρ	850 kg/m^3	σ	1 µm

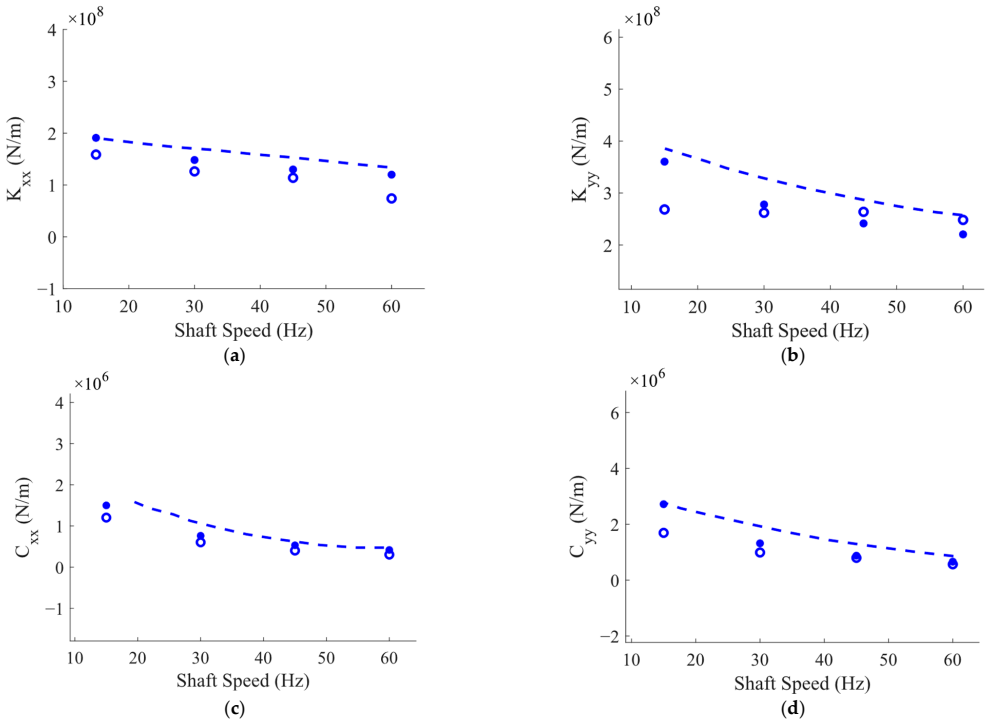

Figure A1. Comparisons of the obtained tilting pad bearing dynamic coefficients with presented experimental results in [65], (**a**) K_{xx} (**b**) K_{yy} (**c**) C_{xx} (**d**) C_{yy} (Asterisk: Prediction from the presented model, Circle: Prediction from Ref. [65], Dashed line: Measurement from Ref. [65]).

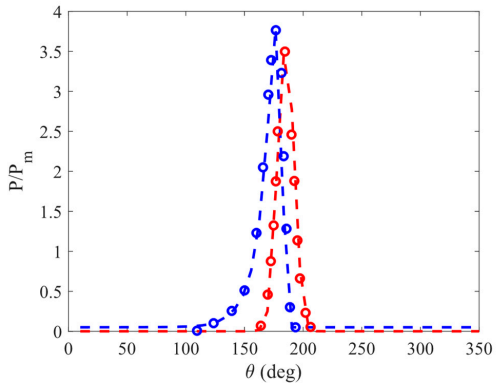

Figure A2. Hydrodynamic and contact pressure distribution for the journal-sleeve worn bearing at Sommerfeld No: 10^{-3} and maximum wear depth of 0.5 C_b. (Red dashed line: Hydrodynamic pressure from the presented model, Blue dashed line: Asperity contact pressure from the presented model, Red circle: Hydrodynamic pressure from Ref. [26], Blue circle: Asperity contact pressure from Ref. [26], $P_m = W_b/(2LR_b)$).

References

1. Ciulli, E.; Forte, P.; Libraschi, M.; Naldi, L.; Nuti, M. Characterization of High-Power Turbomachinery Tilting Pad Journal Bearings: First Results Obtained on a Novel Test Bench. *Lubricants* **2018**, *6*, 4. [CrossRef]
2. Lee, D.; Sun, K.H.; Kim, B.; Kang, D. Thermal Behavior of a Worn Tilting Pad Journal Bearing: Thermohydrodynamic Analysis and Pad Temperature Measurement. *Tribol. Trans.* **2018**, *61*, 1074–1083. [CrossRef]
3. Machado, T.H.; Alves, D.S.; Cavalca, K.L. Investigation about Journal Bearing Wear Effect on Rotating System Dynamic Response in Time Domain. *Tribol. Int.* **2019**, *129*, 124–136. [CrossRef]
4. Dimond, T.; Younan, A.; Allaire, P. A Review of Tilting Pad Bearing Theory. *Int. J. Rotating Mach.* **2011**, *2011*, 908469. [CrossRef]
5. Cloud, C.H.; Maslen, E.H.; Barrett, L.E. Rotor Stability Estimation with Competing Tilting Pad Bearing Models. *Mech. Syst. Signal Process.* **2012**, *29*, 90–106. [CrossRef]
6. Cao, J.; Dimond, T.; Allaire, P. Nonlinear modeling of tilting-pad bearings with application to a flexible rotor analysis. In Proceedings of the International Design Engineering Technical Conferences and Computers and Information in Engineering Conference, Portland, OR, USA, 4 August 2013; American Society of Mechanical Engineers: New York, NY, USA; Volume 55997, p. V008T13A059.
7. Synnegård, E.; Gustavsson, R.; Aidanpää, J.-O. Influence of Cross-Coupling Stiffness in Tilting Pad Journal Bearings for Vertical Machines. *Int. J. Mech. Sci.* **2016**, *111–112*, 43–54. [CrossRef]
8. Kim, S.; Palazzolo, A.B. Bifurcation Analysis of a Rotor Supported by Five-Pad Tilting Pad Journal Bearings Using Numerical Continuation. *J. Tribol.* **2017**, *140*, 021701. [CrossRef]
9. Dixit, H.; Gupta, T.C. Effect of Pad Preload on Fluid Film Coefficients in Tilting Pad Journal Bearing. *Int. J. Sci. Eng. Res.* **2019**, *10*, 139–144.
10. Dang, P.V.; Chatterton, S.; Pennacchi, P. The Effect of the Pivot Stiffness on the Performances of Five-Pad Tilting Pad Bearings. *Lubricants* **2019**, *7*, 61. [CrossRef]
11. Hagemann, T.; Zemella, P.; Pfau, B.; Schwarze, H. Experimental and Theoretical Investigations on Transition of Lubrication Conditions for a Five-Pad Tilting-Pad Journal Bearing with Eccentric Pivot up to Highest Surface Speeds. *Tribol. Int.* **2020**, *142*, 106008. [CrossRef]
12. Bizarre, L.; Andersen, T.B.; Daniel, G.B.; Santos, I.F.; Cavalca, K.L. A 3D Approach for THD Lubrication in Tilting Pad Journal Bearing—Theory and Experiment. *Tribol. Trans.* **2020**, *63*, 120–132. [CrossRef]
13. Yan, K.; Huang, D. Investigation on Static and Dynamic Characteristics of High-Speed and Heavy-Load Tilting Pad Journal Bearings. *Ind. Lubr. Tribol.* **2022**, *74*, 1063–1073. [CrossRef]
14. Soltani, A.; Naderan, H. A Full 3D Computational Model for Tilting-Pad Journal Bearings and Comparing It to 2D Models. *Tribol. Int.* **2021**, *164*, 107223. [CrossRef]
15. Wagner, L.F.; Allaire, P.E. Tilting-Pad Journal Bearings—Frequency-Dependent Dynamic Coefficients and Pivot Flexibility Effects. *Lubricants* **2022**, *10*, 20. [CrossRef]
16. Han, D.; Bi, C.; Chen, C.; Yang, J. Dynamic Coefficients of Tilting Pad Bearing by Perturbing the Turbulence Model. *Appl. Sci.* **2022**, *12*, 6348. [CrossRef]
17. Hojjati, M.; Farzanmehr, S.Y.; Navaz, H.M.; Haddadpour, H. Prediction of Nonlinear Dynamic Coefficients of Tilting-Pad Journal Bearings with Pad Perturbation. *Proc. Inst. Mech. Eng. Part J J. Eng. Tribol.* **2022**, *236*, 1273–1295. [CrossRef]
18. Jin, Y.; Niu, Q.; Qu, Y.; Yuan, X. Pivot Stiffness Effect on Transient Dynamic Characteristic of Tilting Pad Journal Bearing-Rotor System Passing through Critical Speed. *Lubricants* **2023**, *11*, 125. [CrossRef]
19. Shin, D.; Yang, J.; Tong, X.; Suh, J.; Palazzolo, A. A Review of Journal Bearing Thermal Effects on Rotordynamic Response. *J. Tribol.* **2020**, *143*, 031803. [CrossRef]
20. Dufrane, K.F.; Kannel, J.W.; McCloskey, T.H. Wear of Steam Turbine Journal Bearings at Low Operating Speeds. *J. Lubr. Technol.* **1983**, *105*, 313–317. [CrossRef]
21. Gertzos, K.P.; Nikolakopoulos, P.G.; Chasalevris, A.C.; Papadopoulos, C.A. Wear Identification in Rotor-Bearing Systems by Measurements of Dynamic Bearing Characteristics. *Comput. Struct.* **2011**, *89*, 55–66. [CrossRef]
22. Chasalevris, A.C.; Nikolakopoulos, P.G.; Papadopoulos, C.A. Dynamic Effect of Bearing Wear on Rotor-Bearing System Response. *J. Vib. Acoust.* **2013**, *135*, 011008. [CrossRef]
23. Machado, T.H.; Cavalca, K.L. Modeling of Hydrodynamic Bearing Wear in Rotor-Bearing Systems. *Mech. Res. Commun.* **2015**, *69*, 15–23. [CrossRef]
24. Alves, D.S.; Fieux, G.; Machado, T.H.; Keogh, P.S.; Cavalca, K.L. A Parametric Model to Identify Hydrodynamic Bearing Wear at a Single Rotating Speed. *Tribol. Int.* **2021**, *153*, 106640. [CrossRef]
25. Alves, D.S.; Machado, T.H.; da Silva Tuckmantel, F.W.; Keogh, P.S.; Cavalca, K.L. Investigation of Fault Modeling in the Identification of Bearing Wear Severity. *J. Tribol.* **2021**, *144*, 071802. [CrossRef]
26. Kazama, T.; Narita, Y. Mixed and Fluid Film Lubrication Characteristics of Worn Journal Bearings. *Adv. Tribol.* **2012**, *2012*, 296464. [CrossRef]
27. Varney, P.; Green, I. Rotordynamic Analysis of Rotor–Stator Rub Using Rough Surface Contact. *J. Vib. Acoust.* **2016**, *138*, 021015. [CrossRef]
28. Xiang, G.; Han, Y.; He, T.; Wang, J.; Xiao, K.; Li, J. Wear and Fluid-Solid-Thermal Transient Coupled Model for Journal Bearings. *Appl. Math. Model.* **2020**, *85*, 19–45. [CrossRef]

29. Xiang, G.; Wang, J.; Han, Y.; Yang, T.; Dai, H.; Yao, B.; Zhou, C.; Wang, L. Investigation on the Nonlinear Dynamic Behaviors of Water-Lubricated Bearings Considering Mixed Thermoelastohydrodynamic Performances. *Mech. Syst. Signal Process.* **2022**, *169*, 108627. [CrossRef]
30. Cai, J.; Xiang, G.; Li, S.; Guo, J.; Wang, J.; Chen, S.; Yang, T. Mathematical Modeling for Nonlinear Dynamic Mixed Friction Behaviors of Novel Coupled Bearing Lubricated with Low-Viscosity Fluid. *Phys. Fluids* **2022**, *34*, 093612. [CrossRef]
31. Guo, H.; Bao, J.; Zhang, S.; Shi, M. Experimental and Numerical Study on Mixed Lubrication Performance of Journal Bearing Considering Misalignment and Thermal Effect. *Lubricants* **2022**, *10*, 262. [CrossRef]
32. Xiang, G.; Yang, T.; Guo, J.; Wang, J.; Liu, B.; Chen, S. Optimization Transient Wear and Contact Performances of Water-Lubricated Bearings under Fluid-Solid-Thermal Coupling Condition Using Profile Modification. *Wear* **2022**, *502–503*, 204379. [CrossRef]
33. Dang, P.V.; Chatterton, S.; Pennacchi, P.; Vania, A. Effect of the Load Direction on Non-Nominal Five-Pad Tilting-Pad Journal Bearings. *Tribol. Int.* **2016**, *98*, 197–211. [CrossRef]
34. Zhang, Y.; Bingham, C.; Martínez-García, M.; Cox, D. Detection of Emerging Faults on Industrial Gas Turbines Using Extended Gaussian Mixture Models. *Int. J. Rotating Mach.* **2017**, *2017*, 5435794. [CrossRef]
35. da Silva, H.A.P.; Nicoletti, R. Design of Tilting-Pad Journal Bearings Considering Bearing Clearance Uncertainty and Reliability Analysis. *J. Tribol.* **2018**, *141*, 011703. [CrossRef]
36. Lou, M.; Bareille, O.; Chai, W.; Ichchou, M.; Chen, W. Global Sensitivity Analysis of Static Characteristics of Tilting-Pad Journal Bearing to Manufacturing Tolerances. *Tribol. Int.* **2020**, *149*, 105734. [CrossRef]
37. Ranjan, R.; Ghosh, S.K.; Kumar, M. Fault Diagnosis of Journal Bearing in a Hydropower Plant Using Wear Debris, Vibration and Temperature Analysis: A Case Study. *Proc. Inst. Mech. Eng. Part E J. Process Mech. Eng.* **2020**, *234*, 235–242. [CrossRef]
38. Zhou, G.; Qiao, J.; Pu, W.; Zhong, P. Analysis of Mixed Lubrication Performance of Water-Lubricated Rubber Tilting Pad Journal Bearing. *Tribol. Int.* **2022**, *169*, 107423. [CrossRef]
39. Dixit, H.K.; Gupta, T.C. Effect of Geometrical Parameters on Fluid Film Coefficients in Tilting Pad Journal Bearing. *J. Comput. Appl. Res. Mech. Eng.* **2021**, *10*, 405–427. [CrossRef]
40. Niaki, E.T.; Asgharifard-Sharabiani, P.; Ahmadian, H. Bearing Geometric Imperfections Effects on the Rub-Impact Behaviors of a Rotor-Bearing System. In Proceedings of the 26th International Congress on Sound and Vibration, ICSV 2019, Montreal, QC, Canada, 7–11 July 2019. Code 151920.
41. Tofighi-Niaki, E.; Asgharifard-Sharabiani, P.; Ahmadian, H. Nonlinear Dynamics of a Flexible Rotor on Tilting Pad Journal Bearings Experiencing Rub–Impact. *Nonlinear Dyn.* **2018**, *94*, 2937–2956. [CrossRef]
42. Dang, P.V.; Chatterton, S.; Pennacchi, P.; Vania, A. Numerical Investigation of the Effect of Manufacturing Errors in Pads on the Behaviour of Tilting-Pad Journal Bearings. *Proc. Inst. Mech. Eng. Part J J. Eng. Tribol.* **2018**, *232*, 480–500. [CrossRef]
43. Chandra Sharma, S.; Hargreaves, D. A Suitable Method for Journal Bearing Wear Measurement. *Ind. Lubr. Tribol.* **2014**, *66*, 15–22. [CrossRef]
44. Betti, A.; Forte, P.; Ciulli, E. Turbulence Effects in Tilting Pad Journal Bearings: A Review. *Lubricants* **2022**, *10*, 171. [CrossRef]
45. Lv, F.; Jiao, C.; Ta, N.; Rao, Z. Mixed-Lubrication Analysis of Misaligned Bearing Considering Turbulence. *Tribol. Int.* **2018**, *119*, 19–26. [CrossRef]
46. Patir, N.; Cheng, H.S. An Average Flow Model for Determining Effects of Three-Dimensional Roughness on Partial Hydrodynamic Lubrication. *J. Lubr. Technol.* **1978**, *100*, 12–17. [CrossRef]
47. Ng, C.-W.; Pan, C.H.T. A Linearized Turbulent Lubrication Theory. *J. Basic Eng.* **1965**, *87*, 675–682. [CrossRef]
48. Balbahadur, A.C. A Thermoelastohydrodynamic Model of the Morton Effect Operating in Overhung Rotors Supported by Plain or Tilting Pad Journal Bearings. Ph.D. Thesis, Virginia Polytechnic Institute and State University, Blacksburg, VA, USA, 27 February 2001.
49. Asgharifard-Sharabiani, P.; Ahmadian, H. Nonlinear Model Identification of Oil-Lubricated Tilting Pad Bearings. *Tribol. Int.* **2015**, *92*, 533–543. [CrossRef]
50. Knight, J.D. Prediction of Temperatures in Tilting Pad Journal Bearings. *Tribol. Trans.* **1990**, *33*, 185–192. [CrossRef]
51. Greenwood, J.A.; Williamson, J.B.P.; Bowden, F.P. Contact of Nominally Flat Surfaces. *Proc. R. Soc. London. Ser. A. Math. Phys. Sci.* **1997**, *295*, 300–319. [CrossRef]
52. Johnson, K.L.; Greenwood, J.A.; Poon, S.Y. A Simple Theory of Asperity Contact in Elastohydro-Dynamic Lubrication. *Wear* **1972**, *19*, 91–108. [CrossRef]
53. Haneef, M.D.; Randall, R.B.; Smith, W.A.; Peng, Z. Vibration and Wear Prediction Analysis of IC Engine Bearings by Numerical Simulation. *Wear* **2017**, *384–385*, 15–27. [CrossRef]
54. Ma, J.; Zhang, H.; Lou, S.; Chu, F.; Shi, Z.; Gu, F.; Ball, A.D. Analytical and Experimental Investigation of Vibration Characteristics Induced by Tribofilm-Asperity Interactions in Hydrodynamic Journal Bearings. *Mech. Syst. Signal Process.* **2021**, *150*, 107227. [CrossRef]
55. Santos, I.F.; Nicoletti, R.; Scalabrin, A. Feasibility of Applying Active Lubrication to Reduce Vibration in Industrial Compressors. *J. Eng. Gas Turbines Power* **2004**, *126*, 848–854. [CrossRef]
56. Griffini, D.; Salvadori, S.; Meli, E.; Panconi, S.; Ridolfi, A.; Rindi, A.; Martelli, F.; Panara, D.; Baldassarre, L. An Efficient Iterative Coupled Model for the Study of the Insurgence of the Morton Effect in Tilting Pad Journal Bearings. *J. Eng. Gas Turbines Power* **2018**, *141*, 051013. [CrossRef]

57. He, M. Thermoelastohydrodynamic Analysis of Fluid Film Journal Bearings. Ph.D. Thesis, University of Virginia, Charlottesville, VA, USA, 2003.
58. Qiao, G.; Wang, L.; Zheng, T. Linear Stability Analysis of a Tilting-Pad Journal Bearing System. *J. Tribol.* **2006**, *129*, 348–353. [CrossRef]
59. Chen, Y.; Zhang, H.; Li, X.; Xiao, S.; Gu, F.; Shi, Z. Effects of Wear on Lubrication Performance and Vibration Signatures of Rotor System Supported by Hydrodynamic Bearings. *Lubricants* **2023**, *11*, 107. [CrossRef]
60. Wygant, K.D.; Flack, R.D.; Barrett, L.E. Measured Performance of Tilting-Pad Journal Bearings over a Range of Preloads—Part II: Dynamic Operating Conditions. *Tribol. Trans.* **2004**, *47*, 585–593. [CrossRef]
61. Gomez, J.L.; Pineda, S.; Diaz, S.E. On the Effect of Pad Clearance and Preload Manufacturing Tolerances on Tilting Pad Bearings Rotordynamic Coefficients. *Am. Soc. Mech. Eng. Digit. Collect.* **2013**, *55270*, V07BT30A022.
62. Rendl, J.; Dyk, Š.; Smolík, L. Nonlinear Dynamic Analysis of a Tilting Pad Journal Bearing Subjected to Pad Fluttering. *Nonlinear Dyn.* **2021**, *105*, 2133–2156. [CrossRef]
63. Ruggiero, A.; D'Amato, R.; Magliano, E.; Kozak, D. Dynamical Simulations of a Flexible Rotor in Cylindrical Uncavitated and Cavitated Lubricated Journal Bearings. *Lubricants* **2018**, *6*, 40. [CrossRef]
64. Ishida, Y.; Yamamoto, T. *Linear and Nonlinear Rotordynamics: A Modern Treatment with Applications*; John Wiley & Sons: Hoboken, NJ, USA, 2012; ISBN 978-3-527-40942-6.
65. Dmochowski, W.; Brockwell, K. Dynamic Testing of the Tilting Pad Journal Bearing. *Tribol. Trans.* **1995**, *38*, 261–268. [CrossRef]